



An experimental and numerical study of fracture coalescence in pre-cracked specimens under uniaxial compression

Heekwang Lee, Seokwon Jeon*

Department of Energy Systems Engineering, Seoul National University, Gwanak-ro 599, Gwanak-gu, Seoul 151-742, South Korea

ARTICLE INFO

Article history:

Received 23 December 2009

Received in revised form 2 November 2010

Available online 13 December 2010

Keywords:

Crack initiation
Tensile/shear crack
Crack coalescence
DEM
PFC^{2D}

ABSTRACT

This study presents crack initiation, propagation and coalescence at or near pre-existing open cracks or flaws in a specimen under uniaxial compression. The flaw geometry in the specimen was a combination of a horizontal flaw and an inclined flaw underneath. This flaw geometry is different from those reported in the previous studies, where a pair of parallel flaws was used. Three materials were used, PMMA (Poly Methyl MethAcrylate), Diastone (types of molded gypsum), and Hwangdeung granite. Crack initiation and propagation showed similar and different patterns depending on the material. In PMMA, tensile cracks initiated at the flaw tips and propagated to the tip of the other flaw in the bridge area. The cracks then coalesced at a point of the inclined flaw, which is affected by the flaw inclination angle. For Diastone and Hwangdeung granite, tensile cracks were observed followed by the initiation of shear cracks. Coalescence occurred mainly through the tensile cracks or tensile and shear cracks. Crack coalescence was classified according to the crack coalescence types of parallel flaws for overlapping flaw geometry in the past works. In addition, crack initiation and coalescence stresses in the double-flawed specimens were analyzed and compared with those in the single-flawed specimen. Numerical simulations using PFC^{2D} (Particle Flow Code in two dimensions) based on the DEM (Discrete Element Method) were carried out and showed a good agreement with the experimental results in the coalescence characteristics in Hwangdeung granite. These experimental and numerical results are expected to improve the understanding of the characteristics of cracking and crack coalescence and can be used to analyze the stability of rock and rock structures, such as the excavated underground openings or slopes, tunneling construction, where pre-existing cracks or fractures play a crucial role in the overall integrity of such structures.

© 2010 Elsevier Ltd. All rights reserved.

1. Introduction

Rock contains a large number of discontinuities resulting from a variety of geological processes. Pre-existing discontinuities or cracks in rock play important roles in initiating new cracks. When a load is applied, new cracks start to grow at or near the tips of pre-existing cracks and propagate toward the direction of the major principal stress, sometimes coalescing with other cracks. A series of cracking processes eventually control the overall behavior of the rock, which have prompted extensive experimental studies of pre-cracked specimens of different materials, including rock-like brittle/semi-brittle materials and natural rocks: glass (Hoek and Bieniawski, 1965), Columbia Resin 39 (Bombolakis, 1968), Plaster of Paris (Lajtai, 1971, 1974), molded gypsum (Bobet, 2000; Park, 2001; Shen, 1995; Bobet and Einstein, 1998a,b; Reyes and Einstein, 1991; Sagong and Bobet, 2002; Wong and Einstein, 2008a,b), sand-

stone-like material (Mughieda and Alzo'ubi, 2004; Wong and Chau, 1998; Wong et al., 2001), granite (Miller and Einstein, 2008), marble (Park, 2001; Jiefan et al., 1990; Li et al., 2005; Wang et al., 1987), granodiorite (Ingraffea and Heuze, 1980; Wong et al., 2008), limestone (Ingraffea and Heuze, 1980), clay (Vallejo, 1987, 1988), etc. Although there are differences in the crack pattern, common characteristics have been observed: tensile cracks are initiated at the tips of the flaw and propagate in a curvilinear direction with increasing load and shear cracks grow at the tips of the flaw nearly coplanar to the flaw. In particular, Wong and Einstein (2009) reviewed previous studies and suggested that the terminology in the seven different types of the tensile and shear cracking (three types each for tensile and shear cracking and one type of mixed mode cracking) be standardized based on high-speed camera observations rather than by fractography.

Experimental research on a gypsum specimen with a pair of parallel flaws (the term 'flaw' denotes an artificially made pre-existing crack in a specimen) under compression has found a range of crack coalescence patterns according to the nature of crack initiation and coalescence. Shen (1995) reported that three different

* Corresponding author. Tel.: +82 2 880 8807; fax: +82 2 871 8938.

E-mail address: sjeon@snu.ac.kr (S. Jeon).

types of failure occurred depending on the bridge inclination angle: tensile failure, shear failure or mixed-mode failure. Bobet and Einstein (1998a) carried out uniaxial and biaxial compression tests on gypsum specimens with pre-existing cracks and identified five different types of coalescence with a combination of tensile and shearing processes. Wong and Chau (1998) also categorized the crack coalescence patterns in nine cases from the results of a series of uniaxial compression tests. Park (2001) carried out uniaxial compression tests on Diastone (types of molded gypsum) and Yeosan marble with double flawed specimens and identified seven different types of coalescence patterns with tensile, shear, or mixed-mode cracks. Sagong and Bobet (2002) produced three or sixteen flaws in gypsum specimens and carried out uniaxial compression tests to observe the coalescence patterns in double flawed specimens to be extrapolated to multiple flawed specimens. Wong and Einstein (2008a) performed similar experiments on Carrara marble and gypsum using a high-speed camera that could observe the very instant of crack initiation to differentiate shear cracking from tensile cracking. Seven different types of cracking from a single flaw were identified and nine different types of coalescence were classified.

Many numerical methods have been developed to simulate crack initiation and propagation. These numerical methods include the finite element method (FEM), boundary element method (BEM), and displacement discontinuity method (DDM) (Tang et al., 2001). For the last few decades, various criteria were proposed for crack initiation and propagation at the flaw tips. For practical purposes, three criteria are mainly applied (Bobet and Einstein, 1998b; Vásárhelyi and Bobet, 2000): the maximum tangential stress theory (Erdogan and Sih, 1963), maximum energy release rate theory (Hussian et al., 1974), and minimum energy density theory (Sih, 1974). The damage model (Reyes and Einstein, 1991) and F-criterion (Shen and Stephansson, 1994) have been evolved specifically for crack coalescence in the rock bridge area through secondary cracks. Recently, a numerical simulation code, RFPA^{2D} (Rock Failure Process Analysis), was used to simulate crack propagation and coalescence in a rock bridge area. It successfully modeled the global failure of a rock specimen as well as local cracking at the flaw tips (Li et al., 2005; Tang et al., 2001; Tang and Kou, 1998). In addition, DEM (Discrete Element Method) developed by Cundall and Strack (1979) was used to simulate the cracking process in brittle clay specimens (Vesga et al., 2008) and revealed a good agreement with the experimental results. They used PFC^{2D} (Particle Flow Code in two Dimensions) which can reproduce the cracks directly by bond breakage between the circular particles instead of using fracture mechanics theories where complex mathematical equations relevant to the stress intensity factor and fracture toughness at the crack tips are implemented. Therefore, PFC^{2D} was selected as a numerical tool to model the crack propagation and coalescence patterns in this study.

In this study, new double-flaw geometry was introduced to observe crack coalescence in a bridge area. The flaw geometry consisted of a horizontal flaw and an underneath inclined flaw. The new geometry of a double-flaw in this study is expected to improve the understanding of crack propagation and coalescence because en-echelon type of cracks can propagate out of fracture plane to be non-parallel each other according to the orientation of the local stresses as shown in Fig. 1 (Lajitai et al., 1994; Mandal, 1995; Roering, 1968). Three materials for the specimen, such as PMMA (Poly Methyl MethAcrylate), Diastone and Hwangdeung granite, were selected. For each material, the characteristics of crack propagation and coalescence were observed and analyzed. Crack initiation and coalescence stresses in a double-flawed specimen were analyzed and compared with those in the single-flawed specimen. In addition, a numerical simulation using PFC^{2D} was carried out for the Hwangdeung granite specimens.

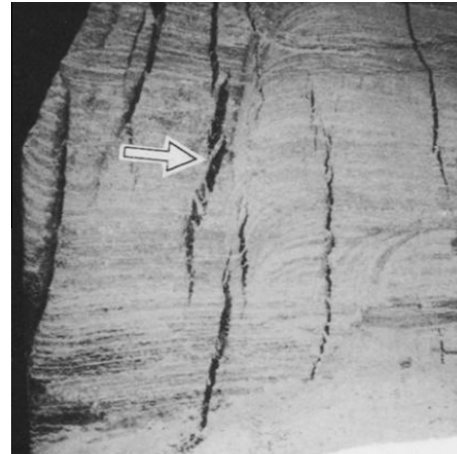


Fig. 1. A photo that contains non-parallel cracks; (a) at a three meter high face of a yield pillar at the Cominco mine in Vanscoy, Saskatchewan (after Lajitai et al., 1994).

2. Specimens and testing apparatus

Both single-flawed and double-flawed specimens were prepared. The flaw geometry in a double-flawed specimen was a combination of a horizontal flaw and an underneath inclined flaw as shown in Fig. 2. The inclined flaw had an inclination angle of 30–90° in 15° intervals. In case of the single-flawed specimens, a flaw inclination angle of 0° was added. The reason why different lengths of flaws were used for different materials as shown in Fig. 2(a) and (b) was to avoid the abrupt rupture of a specimen and not to exceed the loading capacity of the testing facilities. The bridge length of the flaws (2b) as defined in Fig. 2(a) and (b) for different materials was set to 10 mm in order to allow the possible crack coalescence (Bobet and Einstein, 1998a). The procedures for specimen preparation for each material are explained as follows.

Rectangular prismatic specimens of PMMA, 60 × 120 × 25 mm in size, and Hwangdeung granite, 60 × 120 × 30 mm in size, were prepared. A water-jet system was used to produce flaws instead of a diamond saw. High-pressurized water mixed with a garnet abrasive ejected from the 0.75 mm diameter nozzle produced the flaws of 1 mm in aperture thickness. The flaw had rounded tips with a slightly larger aperture thickness at its starting point as shown in Fig. 3(a) and (b) because the water-jet enlarged the hole for the time during which it penetrated the specimen thoroughly. The Diastone specimens of 60 × 120 × 25 mm in size were prepared by mixing Diastone powder and water at the mixing ratio of 1 : 0.26 by weight. The mold with an internal volume of 60 × 120 × 30 mm and covered with two flexible plastic films with two slits at the location of the flaws were used. The flaws of 0.3 mm in aperture thickness were produced by inserting steel shims through the slit after pouring the mixture and removing them after Diastone became hardened. After making flaws, the surfaces of all specimens were polished before the experiment. Fig. 3 shows the PMMA, Diastone, and Hwangdeung granite specimens.

Several specimens with the same flaw geometry were prepared to check out the reproducibility of the test results as summarized in Table 1. The specimen number presents the type of material, number of flaws, flaw inclination angle, and sequential number of specimens. The type of material is presented as A, D and G for PMMA, Diastone, and Hwangdeung granite, respectively, and the number of flaws is expressed as S and D for single and double-flawed specimens in that order. The flaw inclination angle, which is denoted by α , was followed by the sequential number of

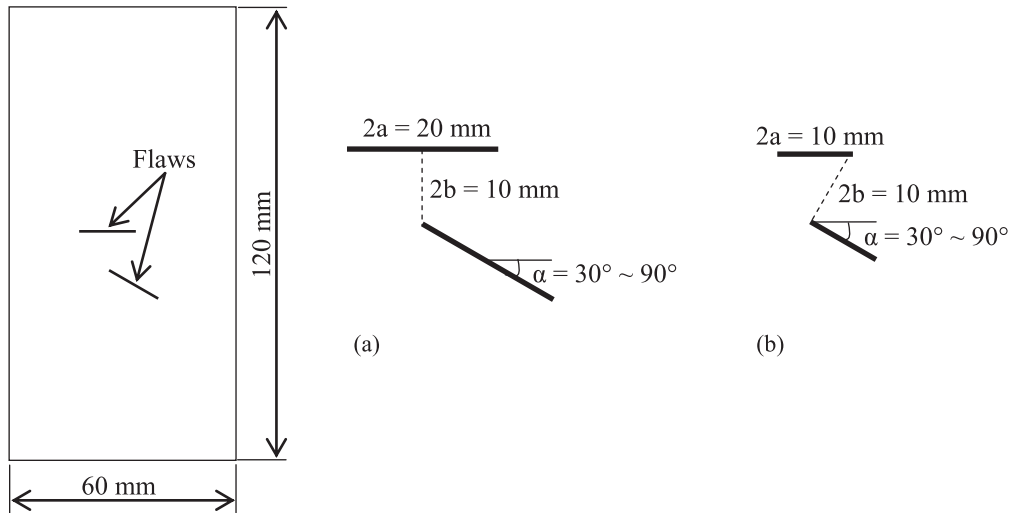


Fig. 2. Schematic plane view of the double-flawed specimen with the flaw geometry: (a) flaw geometry in PMMA and Hwangdeung granite specimens; (b) flaw geometry in Diastone specimens.

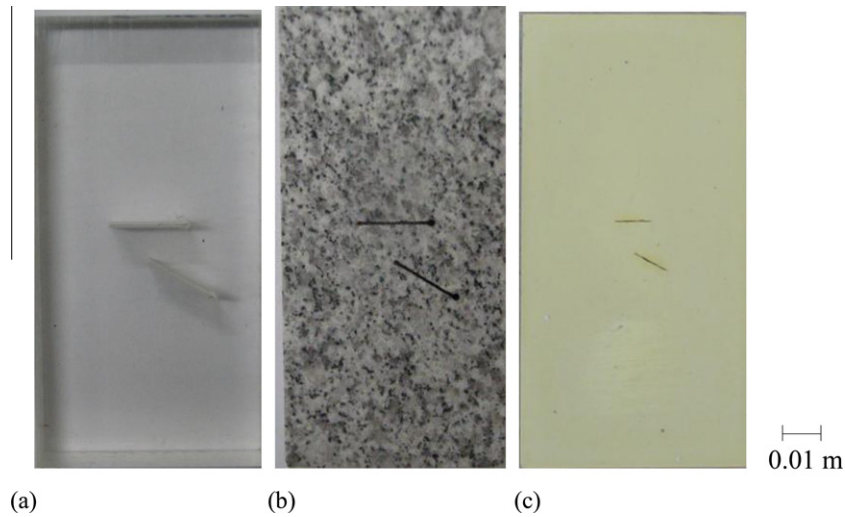


Fig. 3. View of the specimens: (a) PMMA; (b) Hwangdeung granite, and (c) Diastone.

Table 1
Number of specimens of the different materials and configurations.

Flaw type	Flaw inclination angle (α , Degree)	Number of specimens (specimen number)		
		PMMA	Diastone	Hwangdeung granite
Single flaw	0	3 (AS0-1-3)	3 (DS0-1-3)	3 (GS0-1-3)
	30	3 (AS30-1-3)	2 (DS30-1, 2)	3 (GS30-1-3)
	45	3 (AS45-1-3)	1 (DS45-1)	3 (GS45-1-3)
	60	3 (AS60-1-3)	3 (DS60-1-3)	3 (GS60-1-3)
	75	3 (AS75-1-3)	2 (DS75-1, 2)	3 (GS75-1-3)
	90	- ^a	2 (DS90-1, 2)	3 (GS90-1-3)
Double flaw	30	3 (AD30-1-3)	2 (DD30-1, 2)	3 (GD30-1-3)
	45	3 (AD45-1-3)	4 (DD45-1-4)	3 (GD45-1-3)
	60	3 (AD60-1-3)	4 (DD60-1-4)	3 (GD60-1-3)
	75	3 (AD75-1-3)	4 (DD75-1-4)	3 (GD75-1-3)
	90	3 (AD90-1-3)	4 (DD90-1-4)	3 (GD90-1-3)
	Total number		30	31

^a No crack was initiated until the vertical displacement exceeded 10 mm, the capacity of LVDT.

specimens. For example, GD30-2 represents a second, double-flawed Hwangdeung granite specimen with $\alpha = 30^\circ$.

Uniaxial compression tests and Brazilian tensile tests were carried out to obtain mechanical properties of each material. Young's

modulus, UCS (Uniaxial Compressive Strength), Poisson's ratio, and Brazilian tensile strength were obtained by averaging 3–5 laboratory test results, as shown in Table 2. The specimen was loaded until it failed or cracks had coalesced under uniaxial compression.

Table 2
Physical and mechanical properties of PMMA, Diastone, and Hwangdeung granite.

Properties	PMMA	Diastone	Hwangdeung granite
Density, ρ (g/cm ³)	1.18	1.85	2.65
Young's modulus, E (GPa)	2.9	11	55
Uniaxial compressive strength, σ_c (MPa)	139	55	209
Tensile strength, σ_t (MPa)	–	5.0	9.2
Poisson's ratio, ν	0.44	0.28	0.15
Porosity (%)	–	0.15	0.69

Each loading test was recorded using a digital camcorder and a high-speed camera to observe crack initiation, propagation, and coalescence. High-speed camera recorded only the instant of crack coalescence while the digital camcorder recorded the whole loading test. The vertical displacements and applied load were recorded continuously at a rate of 5 Hz. The vertical displacement of the specimen was obtained by averaging measured values from two LVDTs placed on either side of the specimen.

3. Experimental results

3.1. PMMA

3.1.1. Cracks in the single-flawed specimens

In the single-flawed specimens, tensile wing cracks were initiated at the tips of the flaw for all inclination angles less than 90°, as shown in Fig. 4. T_1 and T_2 in Fig. 4(a) were referred to the tensile wing crack. But no crack was initiated with increasing load when the inclination angle was 90°. These cracks propagated curvilinear at first, and then grew in the direction of the major principal stress with increasing load in a stable manner, which means that crack growth stops at the release of the load.

3.1.2. Cracks in the double-flawed specimens

In the double-flawed specimens, tensile cracks were initiated at the tips of the flaws and propagated toward the direction of the major principal stress. In addition, coalescence occurred at or near the tip of the inclined flaw. Table 3 shows the crack coalescence patterns and summarizes the characteristics of the cracks.

For $\alpha = 30^\circ$ and 45° , the tensile crack (T_1) was initiated at the right tip of the inclined flaw at first and grew in a stable manner with increasing load. Then other tensile cracks (T_2 and T_3 for $\alpha = 30^\circ$ and 45° in Table 3) were initiated at the tips of the horizontal flaw. Cracks at the right tip of the horizontal flaw were initiated in both upward and downward directions and the crack in the

downward direction propagated to the left tip of the inclined flaw and coalesced at the tip. After coalescence, other cracks (T_1 and T_{3A} for $\alpha = 30^\circ$; T_1 and T_{2A} for $\alpha = 45^\circ$ in Table 3) initiated from the right tips of both horizontal and inclined flaws grew in a stable manner in the upward and downward directions, respectively.

The crack propagation pattern was quite different for α greater than 45° . First, the coalescence point moved from the left to the right tip of the inclined flaw with increasing α up to 75° . And finally the crack from the horizontal flaw did not meet the inclined flaw for $\alpha = 90^\circ$ as shown in Table 3, which means that no coalescence was made; this crack pattern was similar to that of AS0 specimens as shown in Fig. 4(a). Second, the aperture thickness of the inclined flaw did not decrease with increasing load, as was not the case for α smaller than 60° . This may be because a horizontal flaw shields the inclined flaw from a vertical load. This occurred when the inclined flaw was completely underneath the horizontal flaw for α greater than 60° . This affected the temporal sequence of crack initiation, which means that the cracks were initiated at the tip of the horizontal flaw first not at the tip of the inclined flaw (Compare the locations of T_1 s for $\alpha = 60^\circ$ with those for α smaller than 60° in Table 3).

3.1.3. Stress analysis in PMMA specimens

The crack initiation and coalescence stresses were defined as the stresses when new crack initiation and the crack coalescence were observed with the naked eyes, respectively, in this study. The failure stresses could not be obtained because the PMMA specimens did not fail even after vertical splitting, with bearing the applied load. So the ultimate stresses in Fig. 5 are the stresses when the tests were stopped. A stress drop was observed when the cracks were initiated in the single-flawed specimens for α smaller than 45° and the cracks coalesced in the double-flawed specimens for all α , as shown in Fig. 5(a) and (b). Fig. 6 shows the crack initiation and coalescence stresses. The difference between the magnitude of crack initiation stress and coalescence stress in the double-flawed specimens decreased for α greater than 45° as shown in Fig. 6. The crack initiation stresses in the double-flawed specimens were similar to those of the single-flawed specimens when α was 30° and 45° . However, when α was 60° and 75° , i.e. the inclined flaw was completely beneath the horizontal flaw, the crack initiation stress increased to those of AS0 specimens. This might be because the horizontal flaw had the dominant effect on crack initiation due to shielding of the horizontal flaw against a vertical load (Kranz, 1979; Li et al., 2005). Note that the first crack initiation was observed at the tip of the inclined flaw when $\alpha = 30^\circ$, 45° and at the tip of the horizontal flaw when $\alpha = 60^\circ$, 75° as shown in Table 3. And the effect of the horizontal flaw on the crack initi-

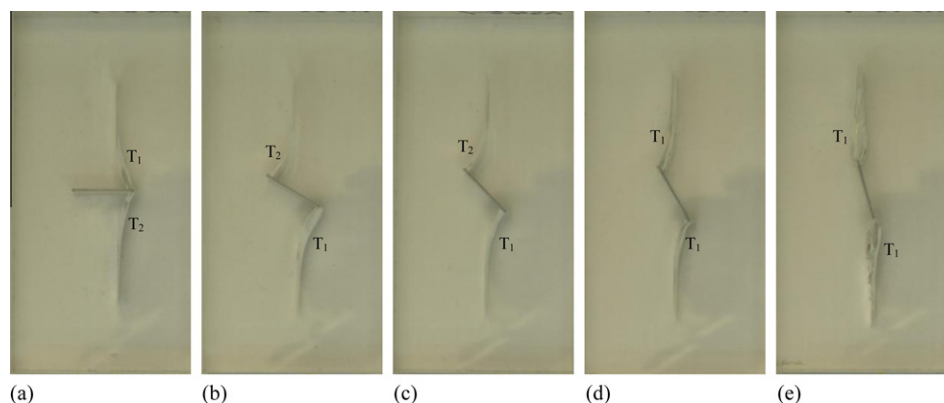
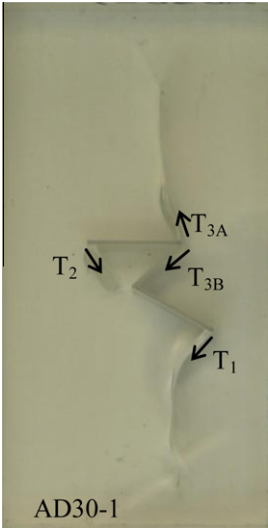
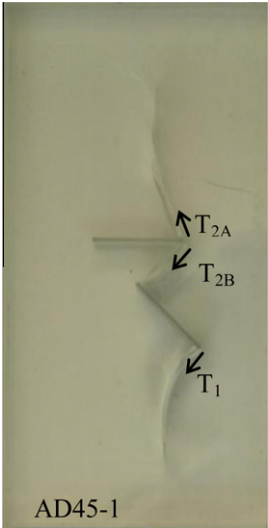
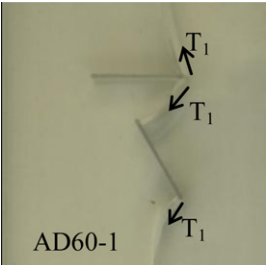
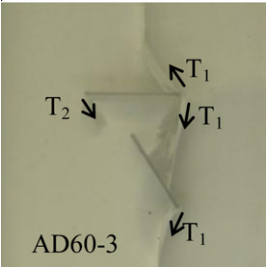
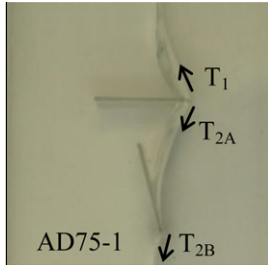
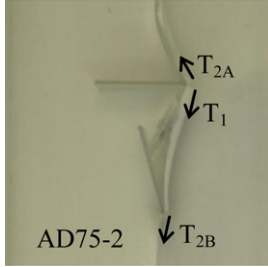
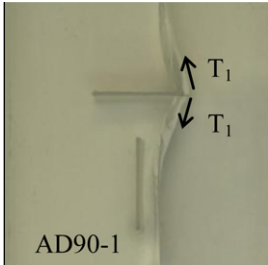
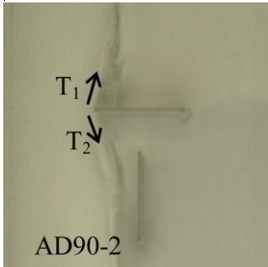


Fig. 4. Cracking patterns in the single-flawed PMMA specimens with different flaw inclination angles: (a) 0°; (b) 30°; (c) 45°; (d) 60°, and (e) 75°. All cracks are tensile cracks. Tensile cracks were identified by T with following subscript number denoting the order of cracking. Two T_1 s in (d) and (e) mean that the cracks were initiated simultaneously.

Table 3
Cracking patterns and characteristics in the double-flawed PMMA specimens.

α (Degree)	30	45	60	75	90
Patterns	 <p>AD30-1</p>	 <p>AD45-1</p>	 <p>AD60-1</p>  <p>AD60-3</p>	 <p>AD75-1</p>  <p>AD75-2</p>	 <p>AD90-1</p>  <p>AD90-2</p>
Characteristics	<ul style="list-style-type: none"> • Tensile cracks were initiated from the flaw tips in the direction of the major principal stress • No shear cracks • Crack was initiated at the right tip of the inclined flaw first • Crack coalescence was observed at the left tip of the inclined flaw • Decrease in the aperture thickness of both the horizontal and inclined flaws with increasing load 		<ul style="list-style-type: none"> • Shielding of the horizontal flaw against vertical stress • No decrease in the aperture thickness of the inclined flaw • Crack coalescence point moved to the right tip of the inclined flaw with increasing α 		<ul style="list-style-type: none"> • No coalescence

T and its subscripts mean tensile crack and the order of crack occurrence, respectively. Also the same number in the subscript means that these cracks were initiated simultaneously.

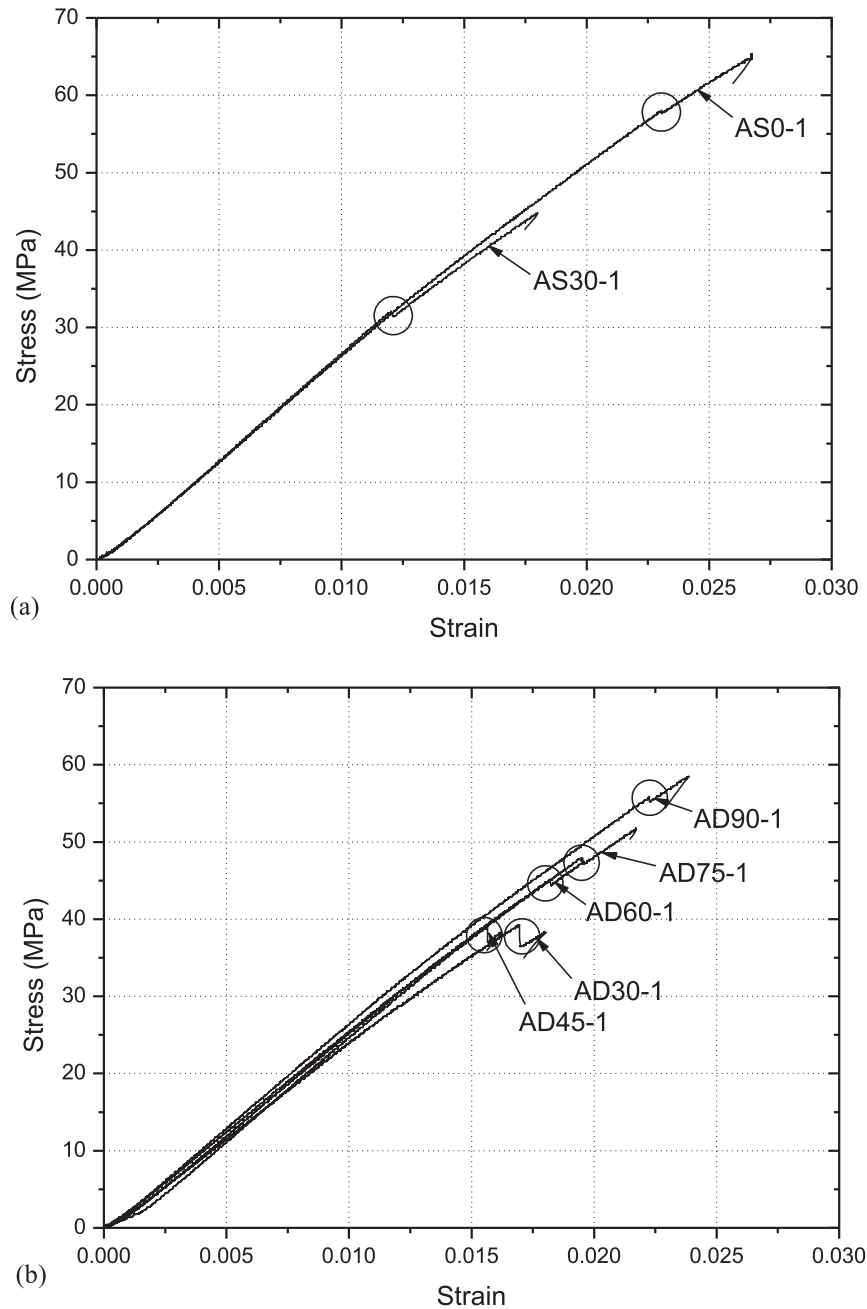


Fig. 5. Stress–strain curves of the PMMA specimen. Note that the stress drop occurred in the circled areas in (a) single flawed specimens (AS0-1 and AS30-1) and (b) double flawed specimens.

ation was bigger than that in the Diastone specimens because the bridge length was smaller than the flaw length, which will be discussed in Section 3.2.3.

3.2. Diastone

3.2.1. Cracks in single-flawed specimens

In the single-flawed specimens, tensile cracks were mainly initiated first followed by shear cracks from the tip of the flaw, which was distinguished by the fractography. The shear crack sometimes emerged from the same flaw tip where the tensile crack had initiated. Specimen failure occurred after the shear cracks had propagated in the coplanar direction with the flaw, as shown in Fig. 7. Curvilinear tensile wing cracks (T_1 , T_2 , and T_3 in Fig. 7(a); T_1 and T_2 in Fig. 7(b)) were observed only when α was 0° and 30° , whereas

a tensile or shear cracks were observed for the other flaw inclination angles. Tensile or shear cracks emanated in a stable manner at the lower compressive load but shear cracks propagated unstably when they were involved with failure at the higher compressive load. Surface spalling was observed adjacent to the tip of the flaw or in the middle of the crack path for $\alpha = 30^\circ$ – 75° , as shown in Fig. 7(b)–(e). This surface spalling means that there is a local compressive stress field (Wong and Einstein, 2008a).

3.2.2. Cracks in double-flawed specimens

Commonly observed coalescence crack was a crack from the middle part of the horizontal flaw to the left tip of the inclined flaw for α larger than 30° . Failure was induced mainly by shear cracks from the horizontal flaw or by a combination of tensile and shear cracks as shown in Table 4. Fig. 8 shows sketches of the cracks with

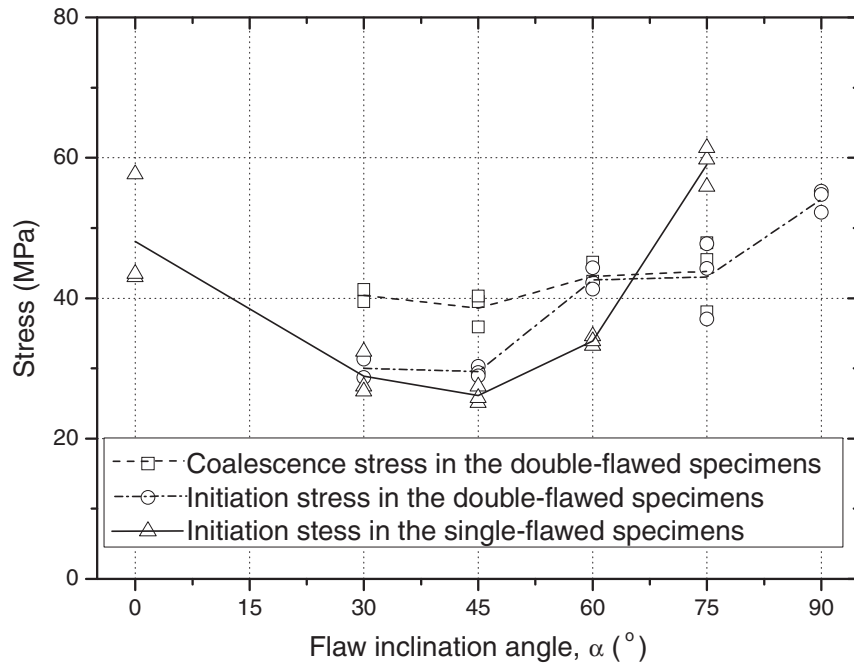


Fig. 6. Crack initiation and coalescence stress versus flaw inclination angle in the single- and double- flawed PMMA specimens. Note that the lines pass through the average values of the stresses for each flaw inclination angle.

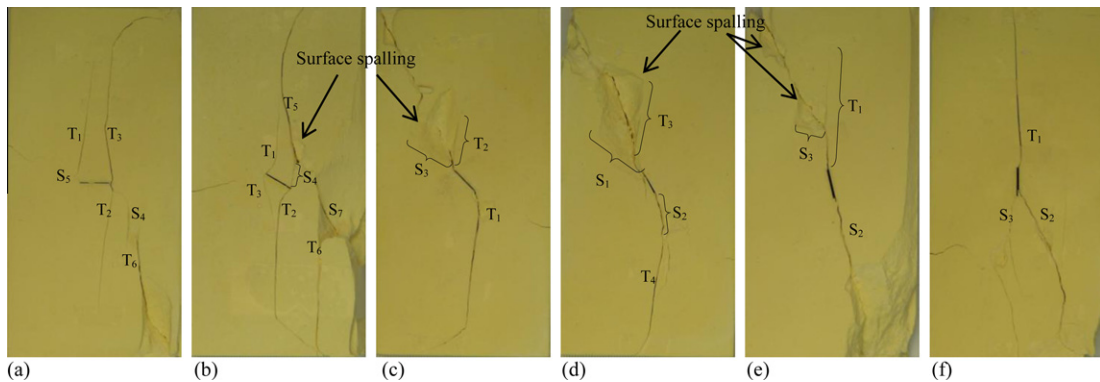


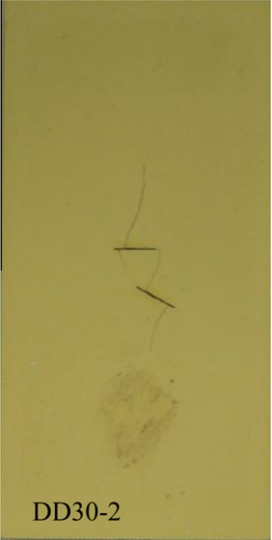
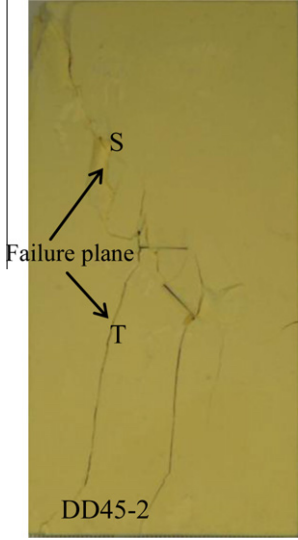
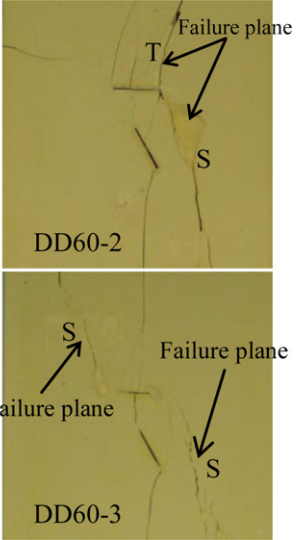
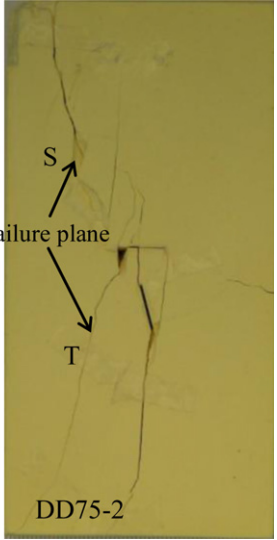
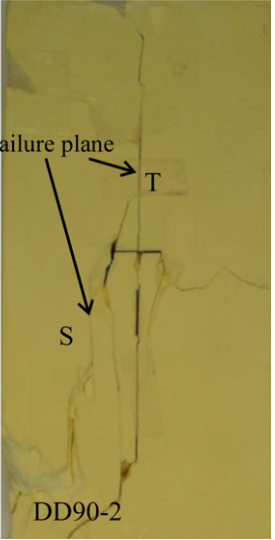
Fig. 7. Cracking patterns in the single-flawed Diastone specimens with different flaw inclination angles: (a) 0°; (b) 30°; (c) 45°; (d) 60°; (e) 75°; and (f) 90°. Tensile cracks and shear cracks are identified by T and S, respectively, with following subscript number denoting the order of cracking.

denoting crack types (T for tensile crack and S for shear crack) and the order of cracking. Table 4 summarizes the characteristics of the cracks and coalescence patterns.

When α was 30° and 45°, tensile cracks were initiated at or near the tips of the horizontal and inclined flaw. Fig. 8(a) and (b) shows sketches of the cracks from flaws when α was 30° and 45°, respectively. Tensile cracks were initiated from or to the tips of the horizontal and inclined flaw, and coalesced at the left tip of the inclined flaw (T_1 of DD30-1 and DD30-2 in Fig. 8(a); T_4 of DD45-1, T_7 of DD45-2, T_4 and T_7 of DD45-3, and T_1 of DD45-4 in Fig. 8(b)) and at the right tip of the horizontal flaw (T_{3A} of DD30-1 and DD30-2 in Fig. 8(a); T_{1B} of DD45-1, T_1 of DD45-2, T_2 of DD45-3, and T_3 of DD45-4 in Fig. 8(b)) for $\alpha = 30^\circ$ and 45°. The cracks not related to coalescence propagated in the direction of the major principal stress, as shown in Table 4. One of the coalescence cracks at $\alpha = 45^\circ$ was a crack from the right tip of the inclined flaw propagated in a direction, opposite to the tensile wing crack from the same tip toward a lower direction, drawing a circular arc and coalescing at the right tip of the horizontal flaw (T_3 of

DD45-1, T_4 of DD45-2, T_5 of DD45-3, and T_5 of DD45-4 in Fig. 8(b)). Shear cracks (S_5 of DD45-1, S_2 of DD45-2, and S_6 of DD45-4 in Fig. 8(b)) were observed at the tips of the horizontal flaw in the coplanar or quasi-planar directions, and failure occurred due to abrupt shear cracking from the left tip of the horizontal flaw to the upper left or lower left corner of the specimen (failure planes for $\alpha = 45^\circ$ as shown in Table 4). For α greater than 60°, the aperture thickness of the inclined flaw did not decrease even though the load had increased and most of the cracks began at the horizontal flaw first rather than at the inclined flaw owing to shielding effect of the horizontal flaw against a vertical load. Coalescence cracks were initiated and propagated from the right tip of the horizontal flaw to the right tip of the inclined flaw when α was 60° and 75° (T_3/S_3 of DD60-1 and S_3 of DD60-3 in Fig. 8(c); T_2 of DD75-1, T_{3A} of DD75-2, T_4 of DD75-3, and T_3 of DD75-4 in Fig. 8(d)), which was the opposite direction to that observed in the specimens for $\alpha = 45^\circ$. For $\alpha = 90^\circ$, coalescence was observed at the crack path as well as at the upper tip of the vertical flaw in DD90-2 (T_5) and DD90-3 (T_{3A}) as shown in Fig. 8(e).

Table 4
Cracking patterns and characteristics in the double-flawed Diastone specimens.

α (Degree)	30	45	60	75	90
Patterns					
Characteristics	<ul style="list-style-type: none"> • Tensile cracks were initiated first from the flaw tips in the direction of the major principal stress • Shear cracks were observed and induced specimen failure • Surface spalling was observed 	<ul style="list-style-type: none"> • Decrease in the aperture thickness of both the horizontal and the inclined flaws with increasing load • Crack propagation from the right tip of the inclined flaw to the right tip of the horizontal flaw 	<ul style="list-style-type: none"> • Shielding of the horizontal flaw against vertical stress • No decrease in the aperture thickness of the inclined flaw • No cracks between the right tip of the horizontal flaw and the left tip of the inclined flaw • Crack propagation from the right tip of the horizontal flaw to the right tip of the inclined flaw 	<ul style="list-style-type: none"> • Vertical splitting • Coalescence at the crack path 	

The crack type is identified by T for tensile crack and S for shear crack.

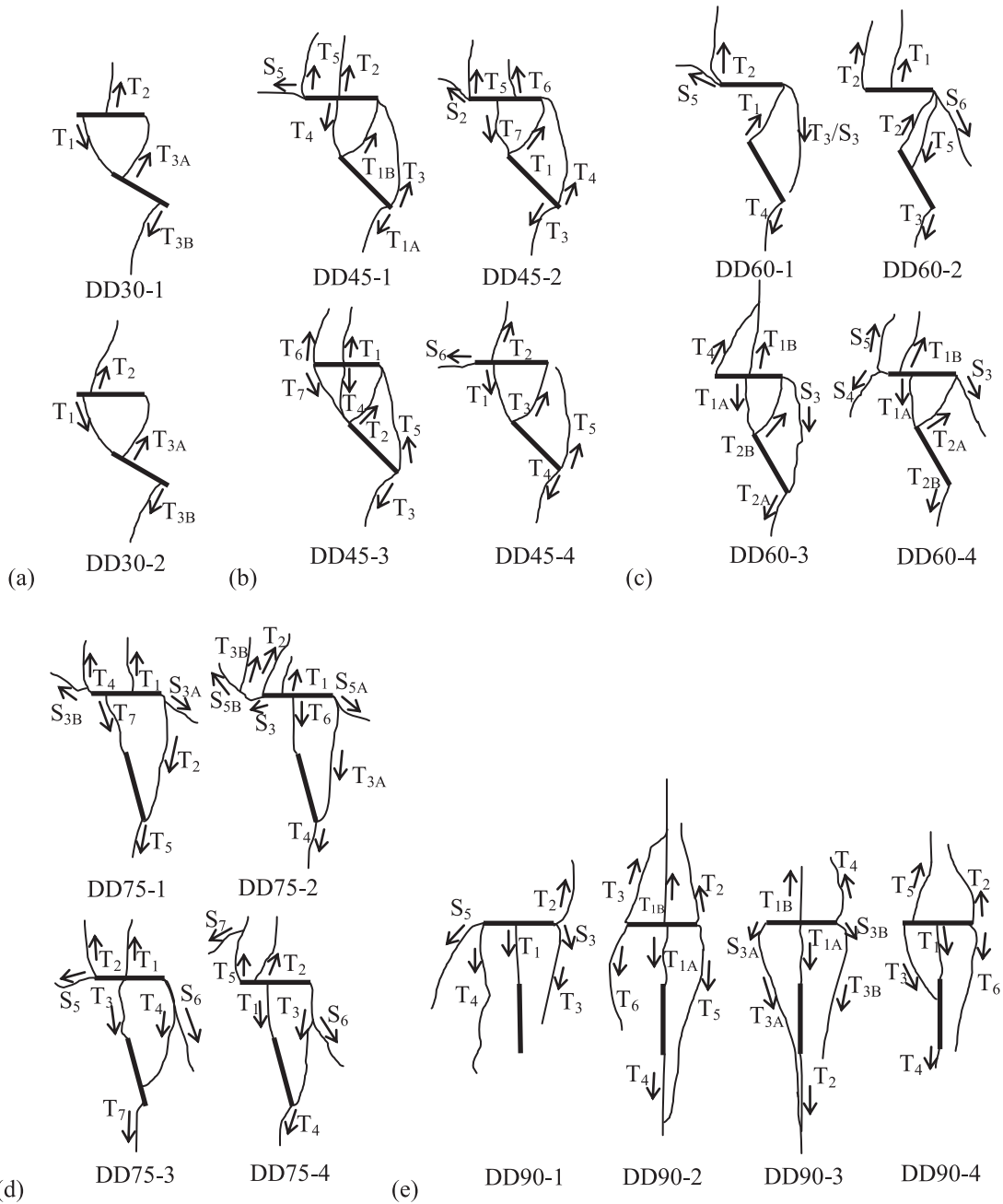


Fig. 8. Sketch of the observed cracks around the bridge area in the Diastone specimens: (a) DD30; (b) DD45; (c) DD60; (d) DD75, and (e) DD90. The thick black lines represent the flaws and the thin lines denote the cracks emanating from the flaws. Tensile cracks and shear cracks are identified by T and S, respectively, with following subscript number denoting the order of cracking.

3.2.3. Stress analysis in Diastone specimens

These tensile wing cracks were initiated at a certain stress level in the single-flawed specimens and a stress drop was observed at the moment for α smaller than 45°, while there was a stress drop in the double-flawed specimens for α bigger than 30° when the cracks coalesced as shown in Fig. 9(a) and (b). The stress drop in the Diastone specimens was not clearly seen as in the case of PMMA specimens (see Fig. 5) because the coalescence process occurred rather gradually. Fig. 10 shows the crack initiation, coalescence, and peak failure stresses. There was an increasing tendency for these stresses in both single and double-flawed specimens, except in the case of the double-flawed specimens for $\alpha = 90^\circ$. The crack initiation stresses of the double-flawed specimens for α smaller than 75° were lower than those of DS0 specimens. However, the level of crack initia-

tion stress for the double-flawed specimens was similar to that of DS0 specimens when α was 75° and 90°. This means that the inclined flaw did not have a great influence on crack initiation due to shielding effect of the horizontal flaw. In addition, the crack initiation stresses in the double-flawed specimens was smaller than those in the single-flawed specimens and the first crack initiation was observed at the tips of the horizontal flaw for most α (see T₁s in Fig. 8), which are the opposite phenomena observed in PMMA specimens shown in Table 5 and Fig. 6, respectively. This may be because the bridge length was larger than that of PMMA specimens, which affect the crack initiation and coalescence. The crack initiation stresses in the double-flawed PMMA specimens when $\alpha = 30^\circ, 45^\circ$ were similar to those in the single-flawed PMMA specimens as was not the case in the Diastone specimens.

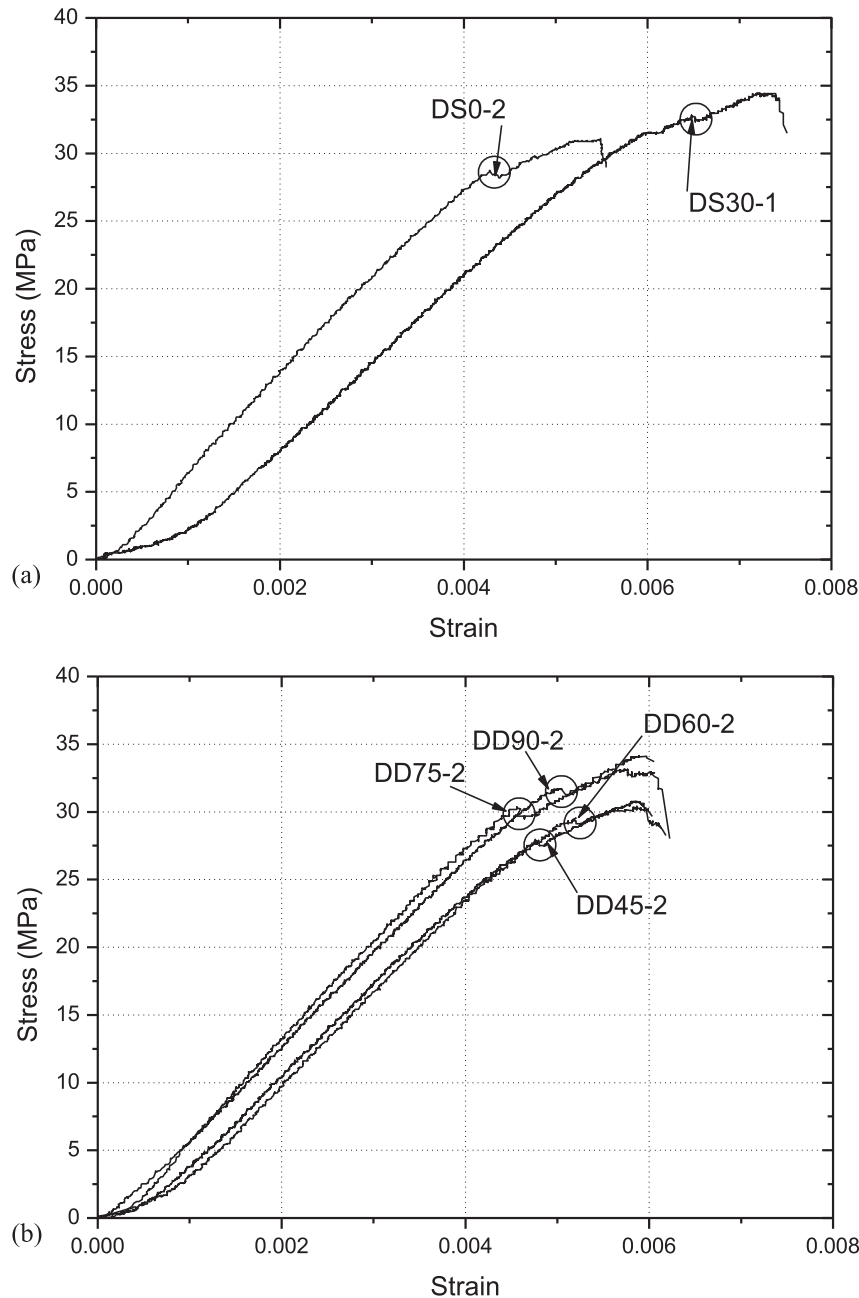


Fig. 9. Stress–strain curves of the Diastone specimens. Note that the stress drop occurred in the circled areas in (a) single-flawed specimens (DS0-2 and DS30-1) and (b) double-flawed specimens.

3.3. Hwangdeung granite

One of the noticeable characteristics observed in granite was a whitening area, which originated adjacent to the flaw tips or an area away from the flaw tip before and after the cracks appeared with increasing load, as shown in Fig. 11. Fig. 11(a) and (b) shows the GD45-1 specimen without and with loading, respectively. The light gray lines shown in Fig. 11(b) denote the whitening areas some of which became cracks. This area was previously referred to white belt (marble specimens in Li et al., 2005) or white patch (Carrara marble in Wong and Einstein, 2008a,b; Barre granite in Miller and Einstein, 2008). The whitening areas lengthened and propagated with increasing load and tensile or shear cracks emerged occasionally (The term ‘white patch’ will be used to denote the whitening area in this study hereafter). However, the

white patch did not always appear where cracks were initiated and vice versa. This means that cracks can initiate along the most favorable direction without any sign of white patch or in spite of another existing one.

3.3.1. Cracks in the single-flawed specimens

In the single-flawed specimens, tensile cracks were initiated mainly from the tips of the flaw. The cracks initiated at the tips of the flaw were tensile cracks in the direction of the major principal stress as shown in Fig. 12. The white patch as a precedent phenomenon was observed before the cracks were initiated and propagated in some cases. In particular, some of the cracks in Fig. 12(d) and (e) were observed in opposite directions only as was not in the case compared with Figs. 4 and 7. This may be because the compression zone of the flaw was developed in the

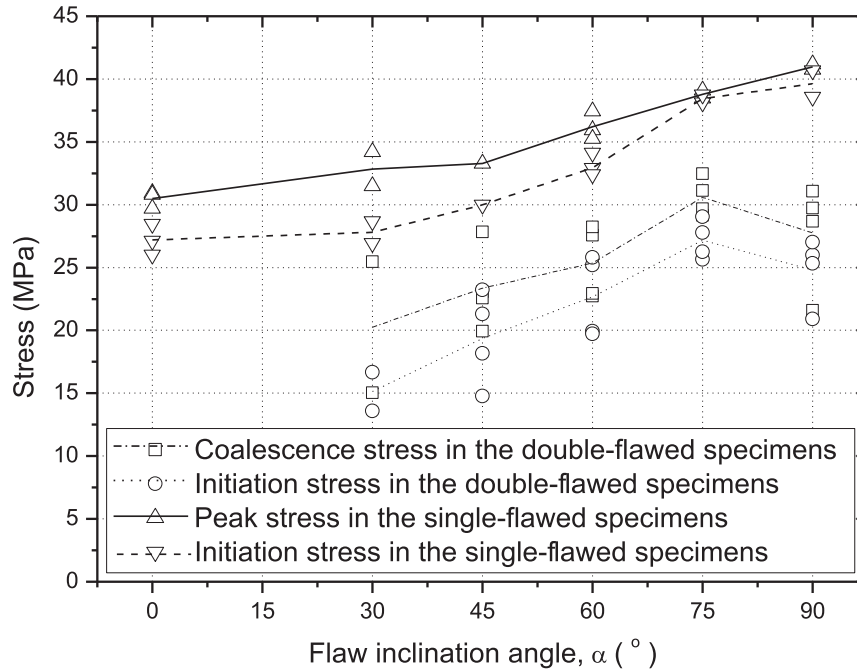


Fig. 10. Crack initiation, coalescence and peak failure stresses versus flaw inclination angle in the single and double-flawed Diastone specimens. Note that the lines pass through the average values of the stresses for each flaw inclination angle.

opposite area to the conventional direction of wing crack as the flaw inclination angle became bigger. This crack was reported as an anti-crack or anti-wing crack (Wong et al., 2008). Vertical splitting occurred for $\alpha = 90^\circ$. Most cracks were tensile but shear cracks were accompanied.

3.3.2. Cracks in double-flawed specimens

In the double-flawed specimens, the crack coalescence patterns were different with respect to α . Fig. 13 shows sketches of the cracks with denoting crack types (T for tensile crack and S for shear crack) and the direction of propagation with an arrow. The order of cracking could not be analyzed even with the help of high-speed camera recording, since cracking occurred too fast in Hwangdeung granite at the frame speed of 1/4000 s with the resolution of 1280×128 pixels. Table 5 summarizes the characteristics of the cracks and the coalescence patterns of the Hwangdeung granite specimens.

When α was 30° (Fig. 13(a)), two tensile cracks were relevant to coalescence: one from the middle of the horizontal flaw to the left tip of the inclined flaw and the other from the middle part of the inclined flaw to the right tip of the horizontal flaw. A shear crack developed at the right tip of the inclined flaw and became a failure plane of the specimen as shown in Fig. 13(a) and Table 5 (GD30-1). Tensile cracks from the left tip or middle part of the horizontal flaw propagated in either upward or downward direction, and reached the boundary of the specimen (see Fig. 13(a) and GD30-1 in Table 5).

In the specimens for $\alpha = 45^\circ$, tensile crack was observed emanating from the right tip of the inclined flaw to the right tip of the horizontal flaw and then shear crack was initiated in the opposite direction toward the right lower corner of the specimen, as shown in Fig. 13(b) and Table 5. The tensile crack from the left tip of the inclined flaw propagated to the right tip of the horizontal flaw. The starting point of this crack is different from that of the crack which started at the middle part of the inclined flaw for $\alpha = 30^\circ$ (compare Fig. 13(a) with Fig. 13(b)).




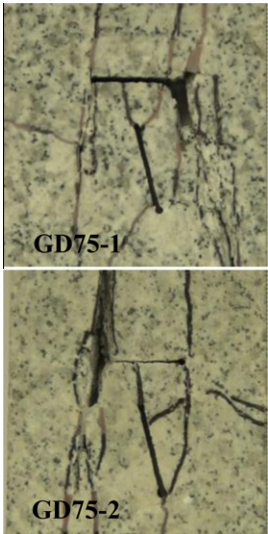

When α was 60° , there were two coalesced cracks; one from the middle part of the horizontal flaw to the left tip of the inclined flaw and the other from the right tip of the inclined flaw to the right tip of the horizontal flaw (Fig. 13(c)). No crack was observed from the left tip of the inclined flaw to the right tip of the horizontal flaw for $\alpha = 60^\circ$. The crack coalescence patterns for $\alpha = 75^\circ$ were similar to those for $\alpha = 60^\circ$ except that crack coalescence between the right tips of the inclined flaw and horizontal flaw did not always occur, such as GD75-1 and GD75-3 in Fig. 13(d). In GD75-2, the coalescence crack was propagated from the right tip of the horizontal flaw to the right tip of the inclined flaw, which is different from that for $\alpha = 45^\circ$ and 60° .

For $\alpha = 90^\circ$, the cracking pattern was similar to the GS0 specimens except for the coalescence crack (compare Fig. 12(a) with GD90-1 in Table 5). The coalescence crack was from the upper tip of the vertical flaw to the middle part of the horizontal flaw and between the cracks from the lower tip of the vertical flaw and from the right tip of the horizontal flaw, as shown in GD90-1 in Fig. 13(e).

3.3.3. Stress analysis in Hwangdeung granite specimens

In the case of Hwangdeung granite, crack initiation and coalescence stresses were observed only in the double-flawed specimens because the crack initiation stress in the single-flawed specimens was hard to detect initiation of the white patch from the digital camcorder in this study. The white patch could represent micro-cracks initiated inside the specimen. Therefore, only the peak stresses are plotted in Fig. 14 for the single-flawed specimens, along with the crack initiation and coalescence stresses for the double-flawed specimens. There was an increasing tendency with increasing α in the single and double-flawed specimens, as shown in Fig. 14. The crack initiation stresses in the double-flawed specimens increased for α smaller than 75° and became almost constant when α was 75° and 90° ; they approached the peak stress of GS0 specimens with increasing α . This again means that the shielding of the horizontal flaw against a vertical load had a dominant effect

Table 5
Cracking patterns and characteristics in the double-flawed Hwangdeung granite specimens.

α (Degree)	30	45	60	75	90
Patterns					
Characteristics	<ul style="list-style-type: none"> • Tensile cracks were initiated from the flaw tips are mostly in the direction of the major principal stress • Failure by only tensile or tensile + shear cracks • White patches were observed before and after crack initiation • Crack propagation from the middle of the inclined flaw to the right tip of the horizontal flaw 	<ul style="list-style-type: none"> • Crack propagation from the left tip of the inclined flaw to the right tip of the horizontal flaw • Crack propagation from the right tip of the inclined flaw to the right tip of the horizontal flaw 	<ul style="list-style-type: none"> • Shielding of the horizontal flaw against vertical stress • No decrease in the aperture thickness of the inclined flaw • No cracks between the right tip of the horizontal flaw and the left tip of the inclined flaw 	<ul style="list-style-type: none"> • Crack propagation from the right tip of the horizontal flaw to the right tip of the inclined flaw 	<ul style="list-style-type: none"> • Vertical splitting • Coalescence at the crack path

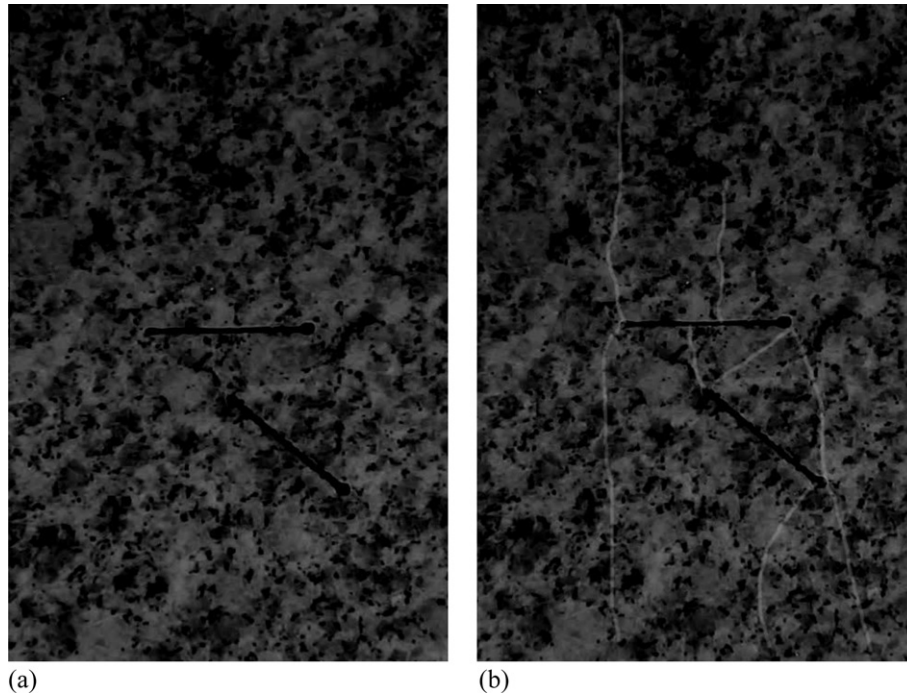


Fig. 11. White patches in GD45-1, drawn in the light gray lines in (b), lengthened along the direction of the major principal stress from the tips of the flaws; (a) $\sigma = 0.0$ MPa; (b) $\sigma = 57.7$ MPa.

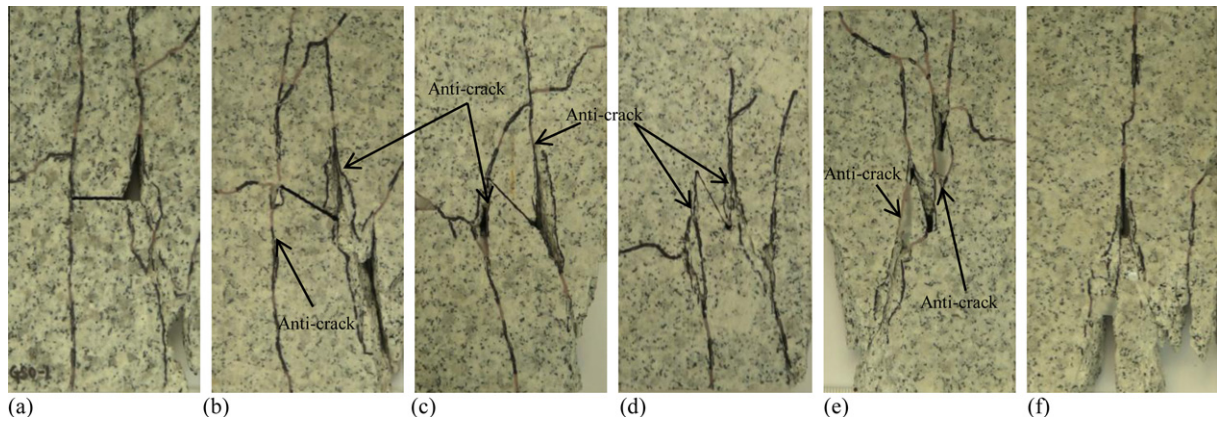


Fig. 12. Cracking patterns in the single-flawed Hwangdeung granite specimens with different flaw inclination angles: (a) 0°; (b) 30°; (c) 45°; (d) 60°; (e) 75°, and (f) 90°. Anti-cracks (Wong et al., 2008) as well as wing cracks were observed in most cases. In some cases, only anti-cracks were developed at higher flaw inclination angles.

on the crack initiation stresses, as the same for PMMA and Diastone specimens.

4. Numerical simulation

4.1. PFC^{2D} and model generation

In the numerical simulation by PFC^{2D}, rock material is represented by an assembly of rigid circular disks bonded together at their contact points. PFC contains two bonding models: a contact-bond model and a parallel-bond model. The parallel-bond has a finite size that acts over either circular or rectangular cross section between the particles, whereas the contact-bond acts only at the contact point due to its vanishingly small size, which can be embodied with the parallel-bond of radius zero. Therefore, the contact-bond can only resist the force acting at the contact, while the parallel-bond can resist both the force and moment. The parallel-

bonds are activated with five parameters, such as normal and shear bond strength, normal and shear bond stiffness, and the bond radius, among which the bond stiffness and bond radius are not assigned in the contact-bond model. The contact/parallel-bonds are broken if the applied stresses are larger than the bond strengths (Itasca, 2002; Potyondy and Cundall, 2004). In the contact-bond model, bond breakage may not affect the macro stiffness significantly provided the particles remain in contact. However, in the parallel-bond model, bond breakage induces an immediate decrease in macro stiffness because the stiffness is contributed by both contact stiffness and bond stiffness. Therefore, the parallel-bond model can be more realistic for rock-like material modeling in which the bonds may break in either tension or shearing with an associated reduction in stiffness (Cho et al., 2007). For this reason, the parallel-bond model was selected in this study.

Several micro parameters should be determined before a parallel-bond model can be generated. These parameters should be

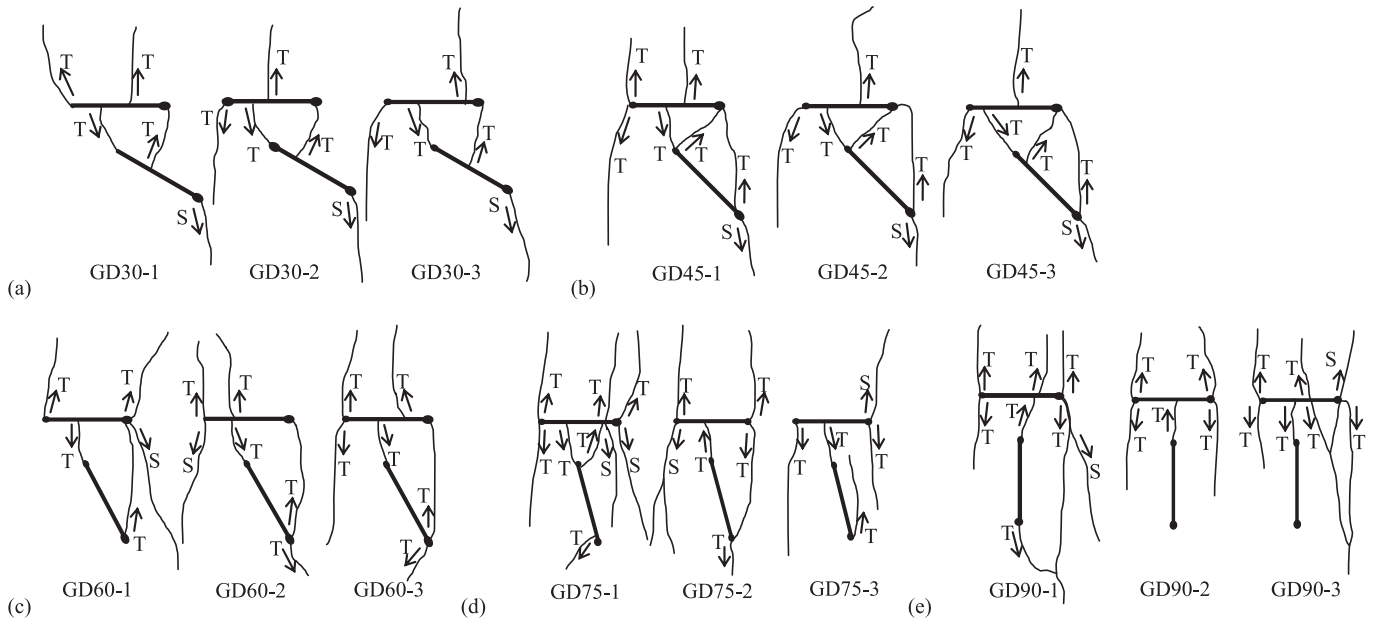


Fig. 13. Sketch of the observed cracks around the bridge area in Hwangdeung granite specimens: (a) GD30; (b) GD45; (c) GD60; (d) GD75, and (e) GD90. The thick black lines represent the flaws and the thin lines denote the cracks emanating from the flaws. Tensile cracks and shear cracks are identified by T and S, respectively, with the direction of propagation.

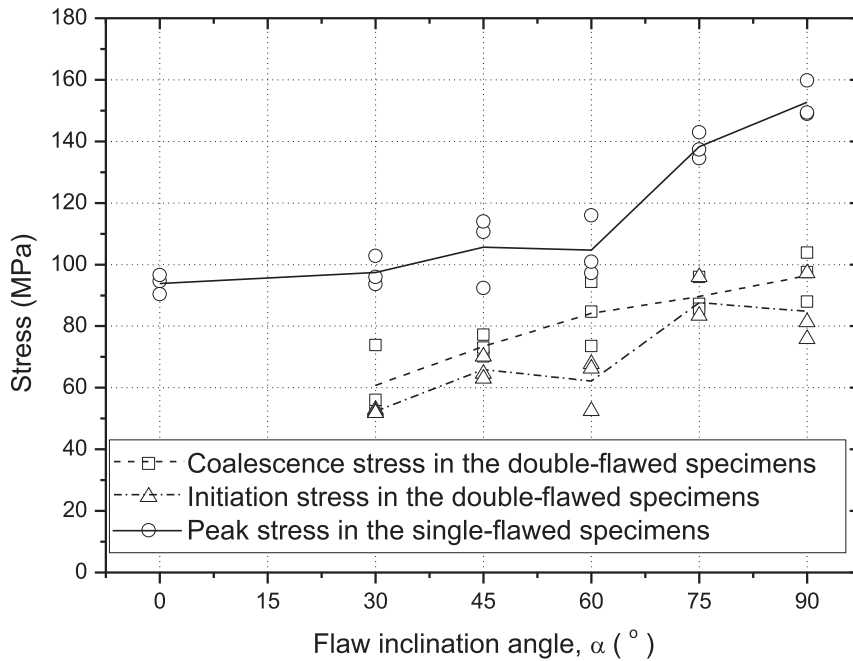


Fig. 14. Crack initiation, coalescence and peak failure stresses versus flaw inclination angle in the single and double-flawed Hwangdeung granite specimens. Note that the lines pass through the average values of the stresses for each flaw inclination angle.

those that make the assembly composed of the different sized circular disks reproduce the macro properties of the real material under uniaxial compression such as Young's modulus, UCS, and Poisson's ratio. A calibration process is required to meet the real physical responses, which is achieved by a "trial and error" process even though some quantitative techniques were proposed with the design of experiment and optimization method etc. (Jong and Lee, 2006; Yoon, 2007). The proposed methods, even if it is a qualitative method, could not produce a model for Hwangdeung granite be-

cause of the limited coverage of the macro properties. The micro parameters in Table 6 were determined throughout the calibration process with a series of sensitivity analysis to give the particle assembly the macro properties shown in Table 2 except for Brazilian tensile strength. Table 6 lists the specified values of the micro parameters for the parallel-bond model for PFC^{2D} including the mean and standard deviations of the macro properties produced from ten UCS tests and Brazilian tensile tests in PFC^{2D}. After generating the model, flaws were created by deleting the particles

Table 6

Micro parameters used for the PFC^{2D} model for Hwangdeung granite specimens and the macro properties tested from the simulations of uniaxial compression test and Brazilian tensile test by PFC^{2D}.

	Values	Remarks	
<i>Micro parameters</i>			
Particle mean radius (mm)	0.30	Uniform distribution	
Particle radius ratio, R_{\max}/R_{\min}	1.66		
Particle density (kg/m ³)	2,650		
Particle contact modulus, E_c (GPa)	37.5		
Particle stiffness ratio, k_n/k_s	1.2		
Parallel-bond radius multiplier	1.0		
Parallel-bond modulus, E_c (GPa)	37.5		
Parallel-bond stiffness ratio, k_n/k_s	1.2		
Particle friction coefficient	0.5		
Parallel-bond normal strength, mean (MPa)	160		Normal distribution
Parallel-bond normal strength, std. dev. (MPa)	43.2	27% of mean value	
Parallel-bond shear strength, mean (MPa)	320	Normal distribution	
Parallel-bond shear strength, std. dev. (MPa)	86.4		
<i>Macro properties</i>			
Young's modulus (GPa)	56.42 ± 0.47	Mean and standard deviation from 10 repetitive tests in PFC ^{2D}	
Poisson's ratio	0.1531 ± 0.0087		
UCS (MPa)	206.83 ± 13.99		
Tensile strength (MPa)	40.28 ± 3.50		

aligned at the location of the flaw. The size of the model was 60 × 120 mm and was composed of approximately 12,000 particles.

4.2. Simulation results

Figs. 15 and 16 show the crack coalescence in the single and double-flawed model after the peak stress in the PFC^{2D} simulation, respectively. The black and red dots shown in Figs. 15 and 16 represent the micro cracks formed as a result of the tensile and shear contact force exceeding the prescribed parallel-bond normal and shear strength, respectively. The overall formation of the cracks showed a good agreement with the experimental results. The cracks emanated from the tips of the flaw and propagated toward the direction of the major principal stress.

In the single-flawed model shown in Fig. 15, the direction of initiation and propagation was similar to the experiment when α was 30–60° (Fig. 15(b)–(d)). The cracks were in the direction of the major principal stress in most cases, even though some of the cracks were in a direction between that of the major principal stress and flaw plane. Crack clusters were observed at the corner edge of the specimens which was not observed in the real rock specimens. These phenomena are believed to be analogous to the observed white patch that did not grow to a visible crack. In addition, the exact crack propagation path could not be obtained due to the nature of this kind of testing and simulation. However, the overall pattern of cracking could be simulated in the PFC^{2D} model. When α was greater than 75°, the crack propagation paths deviated to the direction of the shear failure plane as well as to the vertical direction (Fig. 15(e) and (f)).

In the double-flawed models shown in Fig. 16, the crack paths were generally similar to those of the experimental results. When α was 30°, the crack paths were almost along the real ones except for the cracks from the right tip of the inclined flaw, which propagated toward the side edge of the specimen while the real crack propagated downward. Another crack emanating from the right tip of the inclined flaw also denoted the direction of the white patch that existed but did not grow into a visible crack. As α increased to 45–75°, crack clusters along the flaw plane were simulated but were not observed in the real specimens, as shown in Fig. 16(b)–(d). The crack propagation paths in the models with the vertically inclined flaw showed a close resemblance to the test results, as shown in Fig. 16(e). All the numerical simulations using PFC^{2D} could be different from each other depending on how the

particle assembly was generated. The results shown in Figs. 15 and 16 were extracted from ten simulations carried out on ten different models generated from different seed numbers for random particle packing.

Fig. 17 shows the crack initiation, coalescence, and peak failure stresses in single and double-flawed specimens in numerical simulations. The crack initiation and coalescence stresses in double-flawed specimens in PFC^{2D} had the similar trend with the increasing α , which shows the differences in values of the experimental tests and numerical simulations. In numerical simulation, the crack initiation stress decreased with increasing α from 30° to 60° and increased after α was bigger than 60°, which was not clearly observed in experimental tests. In single-flawed specimens, the peak failure stresses showed the similar pattern but the values of the numerical simulation were bigger than those of experiment by 21–33%. This may be because the numerical simulation was two dimensional analyses by synthetic materials composed of many circular disks, which cannot exactly simulate the three dimensional physical phenomena of heterogeneous rock specimens such as Hwangdeung granite.

5. Discussion

The new flaw geometry examined in this study was analogous to the overlapping flaw geometry reported by Wong and Chau (1998), Sagong and Bobet (2002), and Wong and Einstein (2008a). The coalescence patterns observed in this study could be compared with those in the previous studies. Wong and Chau (1998) classified the coalescence patterns into nine categories, five of which were relevant to the overlapping geometry, and reported that the nature of the coalescing crack were mainly tensile (Fig. 18(a)). Sagong and Bobet (2002) also classified them into nine categories, four of which were relevant to the overlapping geometry, as shown in Fig. 18(b). Wong and Einstein (2008a) showed that the precise nature of a coalescing crack could be included in their coalescence categories using a high-speed camera, as shown in Fig. 18(c). Table 7 summarized the crack coalescence type by the classification shown in Fig. 18(a)–(c).

In PMMA, tensile cracks propagated from the right tip of the horizontal flaw and coalesced at the left tip of the inclined flaw when α was smaller than 60°. The coalescence cracks were observed on the side of high flaw density, which means that the cracks coalesced between the closest tips, particularly on the right side of the flaw geometry (Table 3). The coalescence point moved

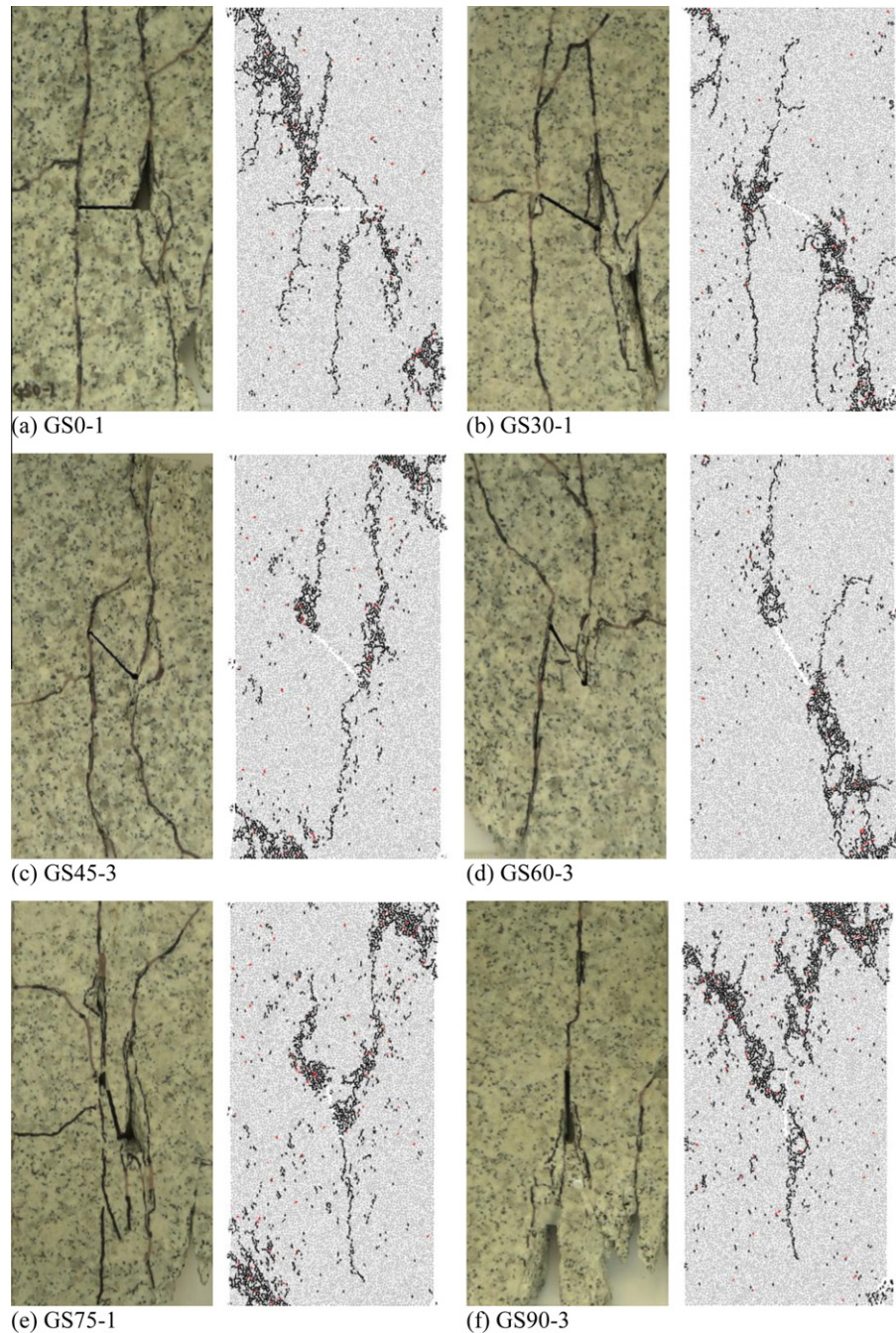


Fig. 15. Crack propagation and coalescence in the single-flawed Hwangdeung granite specimens from the experiments and PFC^{2D} simulations. Note that the black thick lines on the real specimen surface were drawn along the cleavage of a newly formed crack. The black and red dots denote the tensile and shear micro cracks in the PFC^{2D} model, respectively.

to the right tip with increasing α , but the crack did not coalesce when α was 90° . These coalescence cracks could be in categories WI, WII, or WIII reported by Wong and Chau (1998), in category IV suggested by Sagong and Bobet (2002), or in categories 6, 7, or 8 according to Wong and Einstein (2008a), as shown in Table 7.

In Diastone, several cracks were observed involving coalescence in a bridge area. The coalescence cracks originated from the left tip of a horizontal flaw to the left tip of an inclined flaw, from the middle part of a horizontal flaw to the left tip of an inclined flaw, from the left tip of an inclined flaw to the right tip of a horizontal flaw, and finally from the right tip of a horizontal flaw to the right tip of an inclined flaw, as shown in Fig. 8. These coalescence cracks could

be in categories WI, WII, WIII, WI/III, or WII/III reported by Wong and Chau (1998), in category IV proposed by Sagong and Bobet (2002), or in categories 6, 7, or 8 according to Wong and Einstein (2008a), as shown in Table 7.

In Hwangdeung granite, the crack propagation patterns were similar to Diastone but the crystalline granular structure affected the cracking process, as indicated by the white patch described in Section 3.3. The coalescing cracks were from the middle part of a horizontal flaw to the left tip of an inclined flaw, from the middle part of an inclined flaw to the right tip of a horizontal flaw, from the left tip of an inclined flaw to the right tip of a horizontal flaw, and from the right tip of a horizontal flaw to the right tip of an inclined flaw, as shown in Fig. 13. These coalescence cracks could

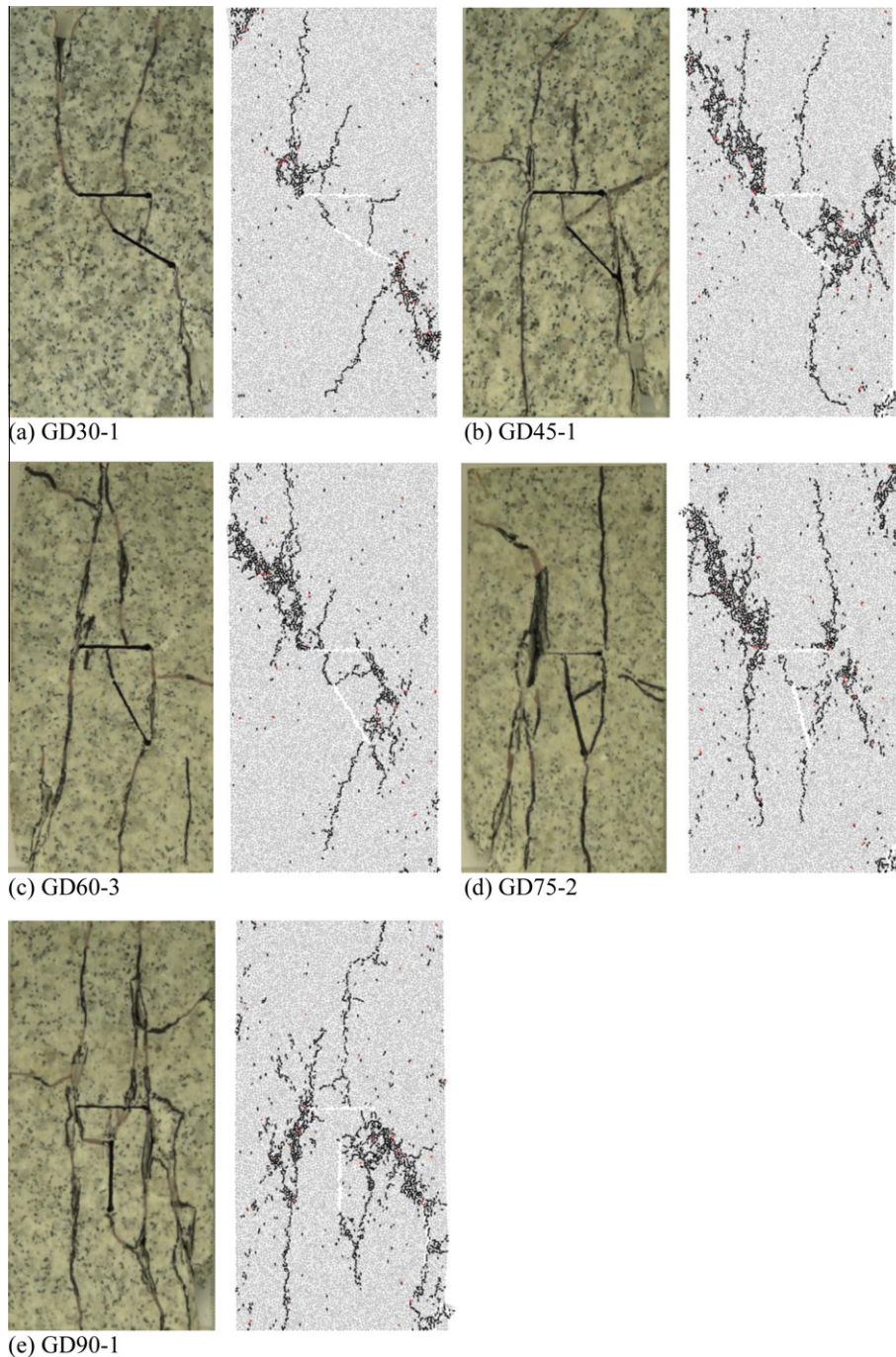


Fig. 16. Crack propagation and coalescence in the double-flawed Hwangdeung granite specimens from the experiments and PFC^{2D} simulations. Note that the black thick lines on the real specimen surface were drawn along the cleavage of a newly formed crack. The black and red dots denote the tensile and shear microcracks in the PFC^{2D} model, respectively.

be in categories WI, WII, WIII, or WII/III reported by Wong and Chau (1998), in category IV suggested by Sagong and Bobet (2002), or in categories 6, 7, or 8 according to Wong and Einstein (2008a), as shown in Table 7. For $\alpha = 90^\circ$, one of the coalescence cracks was in category 2 of indirect coalescence according to Wong and Einstein (2008a) as with Diastone.

The crack coalescence categories by Sagong and Bobet (2002) involved shear cracks and tensile cracks that were not observed in this study throughout all materials. The only Type IV denoted the coalescence by the tensile wing crack, which can explain some of the observations. Table 7 shows only category IV among the coalescence types reported by Sagong and Bobet (2002).

Since the rock bridge length was relatively small compared to the flaw length, the coalescence types could be different from those of previously reported, in that the bridge length was usually larger than the flaw length. The bridge length ratios of the Hwangdeung granite and Diastone were $0.5a$ (10/ 20 mm) and $1.0a$ (10/ 10 mm), respectively. This affected the coalescence types, which means that the starting points of the coalescence crack in the Hwangdeung granite and Diastone specimen were at the middle point and left tip of the inclined flaw, respectively (see Fig. 8(a) and Fig. 13(a)). This result was consistent with the previous works that the bridge length less than $1.5a$ influence the coalescence type between the tips of the adjacent flaws (Wong and Chau, 1998). It

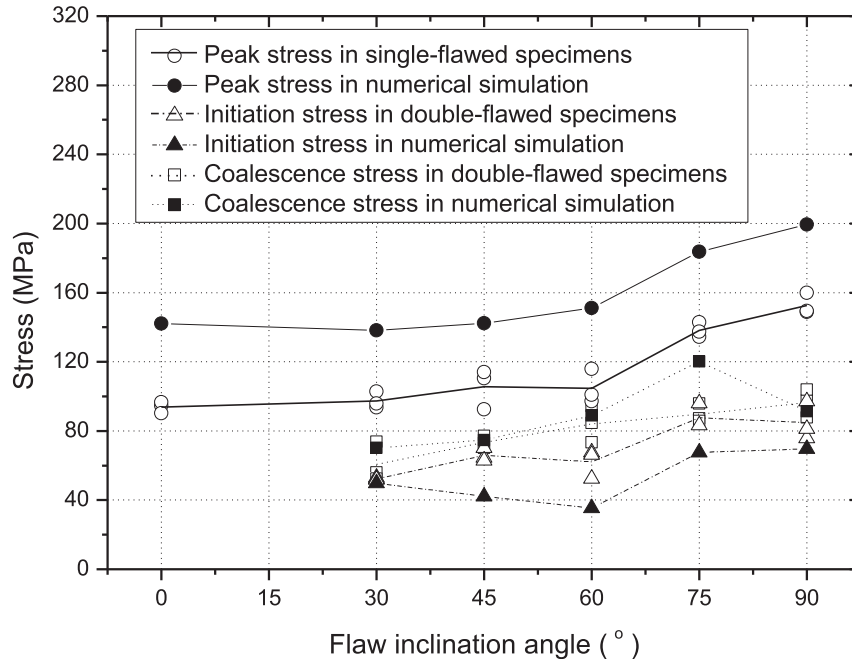


Fig. 17. Crack initiation, coalescence and peak failure stresses versus flaw inclination angle in the single and double-flawed Hwangdeung granite specimens in both experimental test and numerical simulation (PFC2D).

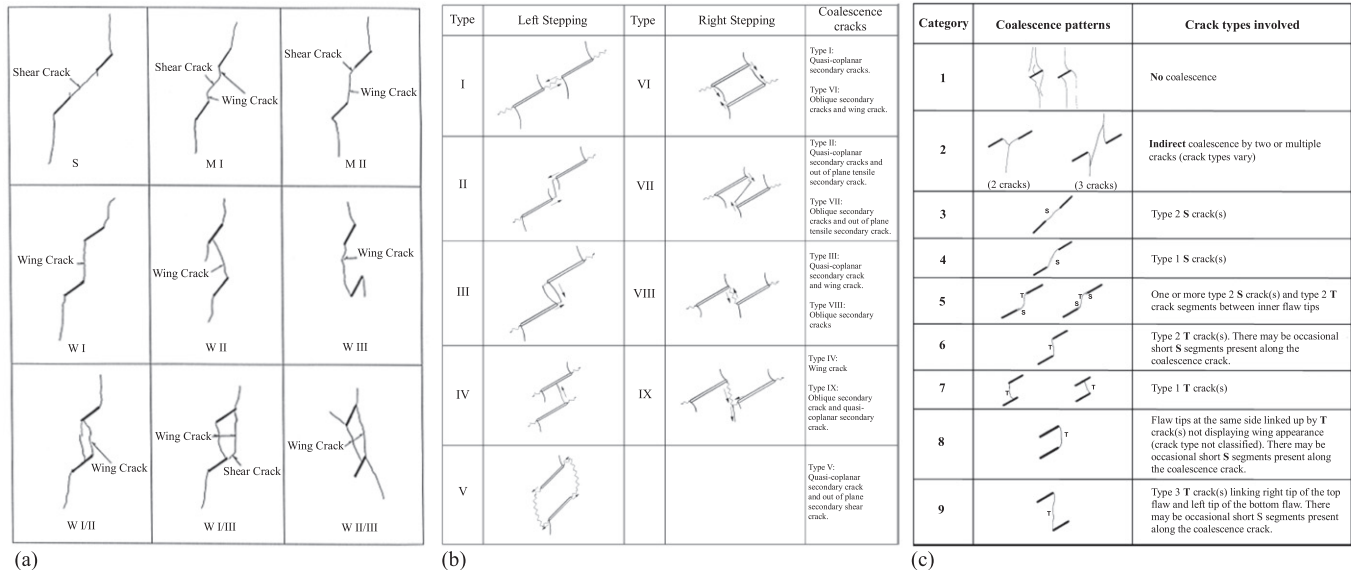


Fig. 18. Classification of the coalescence types in the previous studies. These included the non-overlapping flaw geometry as well as the overlapping flaw geometry: (a) Wong and Chau (1998); (b) Sagong and Bobet (2002), and (c) Wong and Einstein (2008a).

was observed that the crack initiation stresses in PMMA and Diastone specimens were affected by the bridge length and the shielding effect of the horizontal flaw. As explained in Sections 3.1.3 and 3.2.3, the crack initiation stresses in different bridge length made sure that there was some effect of the bridge length and the horizontal flaw on the crack initiation. However, the effect of the bridge length ratio could not be fully discussed because fixed bridge length ratios were used with respect to each material throughout this study. Further study should be carried out on the effect of the various bridge lengths and the cracking mechanism of the horizontal flaws. In addition, the shear cracks that were not involved in coalescence developed mainly from the tips of

the horizontal flaw as a failure plane across the Diastone and Hwangdeung granite specimens, as shown in Fig. 19. Shear cracks initiated after the initiation of tensile cracks and sometimes surface spalling preceded shear cracks particularly in Diastone.

The shielding of the horizontal flaw against a vertical load was observed when the inclined flaw was completely beneath the horizontal flaw, i.e. α was greater than 60° for all materials. This shielding effect prevented the aperture thickness of the inclined flaw from decreasing with increasing load. In this case, for the Diastone and Hwangdeung granite specimens, the cracks initiated at the horizontal flaw tips first and then at the inclined flaw tips. For $\alpha = 90^\circ$, coalescence occurred at a point in the cracks not in

Table 7

Classification of the crack coalescence patterns observed in this study using the classification in the previous studies shown in Fig. 18.

α (Degree)	Wong and Chau (1998)			Sagong and Bobet (2002)			Wong and Einstein (2008a)		
	PMMA	Diastone	Hwangdeung granite	PMMA	Diastone	Hwangdeung granite	PMMA	Diastone	Hwangdeung granite
30	WI	WI/III	WII	–	–	IV ^d	6	6, 8	7
45	WI	WI, WII, WIII ^a	WI, WII, WIII ^a	–	IV ^d	IV ^d	6	6, 7, 8	6, 7, 8
60	WI, WII	WI, WII, WIII ^a	WII/III	IV ^b	IV ^d	IV ^d	6, 7	6, 7, 8	7, 8
75	WII, WIII	WII/III	WII/III	IV ^b	IV ^d	IV ^d	7, 8	7, 8	7, 8
90	– ^c	WII	WII	– ^c	IV ^d	IV ^d	1	2, 7	2, 7

^a The coalescence patterns were observed in all specimens.

^b The category IV covers only one of the coalescence types observed in PMMA specimens. Refer to Table 3 for PMMA specimens.

^c No coalescence.

^d Only a tensile crack from the left tip of the inclined flaw to the middle of the horizontal flaw can be included in the category IV. Refer to Table 4 (or Fig. 8) and Table 5 (or Fig. 13) for Diastone and Hwangdeung granite specimens, respectively.

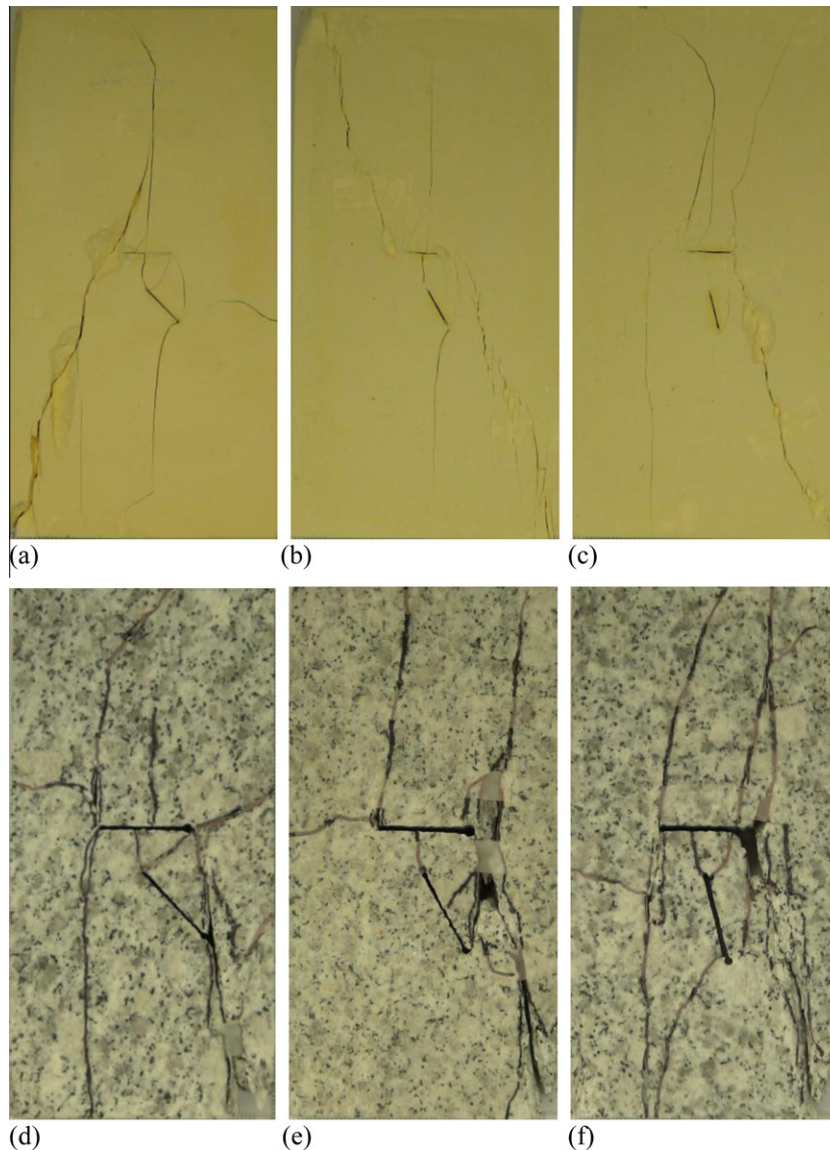


Fig. 19. Failure planes created by the shear cracks in the Diastone and Hwangdeung granite specimens: (a) DD45-1; (b) DD60-3; (c) DD75-4; (d) GD45-1; (e) GD60-1, and (f) GD75-1.

the flaw tip, as shown in DD90-2, 3 in Fig. 8(e) and GD90-1 in Fig. 13(e). In PMMA, no coalescence was observed as in AD90-1, 2 in Table 3. Table 8 summarizes the common and different features of the cracking processes depending on the materials.

The numerical simulations demonstrated that the PFC^{2D} based on DEM could reproduce the crack initiation and propagation process with increasing load directly by means of bond-breakage without introducing complicated mathematical relations involving

Table 8
Characteristics of the cracks depending on the material.

	PMMA	Diastone	Hwangdeung granite
Common characteristics	<ul style="list-style-type: none"> • Crack propagation in the direction of the major principal stress • Coalescence by the tensile cracks • Shielding of the horizontal flaw against the vertical load when α was greater than 60° • No crack penetration into the horizontal flaw 	<ul style="list-style-type: none"> • Similar crack coalescence patterns with the flaw inclination angle, α • Shear cracks emerged • Failure occurs by tensile or shear + tensile cracks • Coalescence at the crack path and axial splitting for $\alpha = 90^\circ$ • Surface spalling 	<ul style="list-style-type: none"> • Elongation of the white patches before and after the crack initiation with the load
Differences	<ul style="list-style-type: none"> • Only tensile cracks were initiated • Crack coalescence point moved to the right tip of the inclined flaw with increasing α • No crack coalescence at $\alpha = 90^\circ$ 		

a stress intensity factor or fracture toughness. However, the micro parameter calibration, which is essential for model generation, was needed before the uniaxial compression tests in PFC^{2D}. The general cracking process under uniaxial compression in hard crystalline rock, i.e. Hwangdeung granite, was simulated successfully except for additional cracks in the direction parallel or sub-parallel to the flaw plane. The reason why the simulations were not carried out on the PMMA and Diastone specimens was because it was difficult to reproduce the cracking behavior of an amorphous structure (PMMA) or a relatively homogeneous continuum material (Diastone) using a synthesized assembly composed of circular disks. Crack initiation and coalescence stresses in the numerical simulation showed similar patterns with the experimental results in double-flawed specimens but there were differences in values.

6. Conclusions

Uniaxial compression tests were carried out on three different types of specimens containing single and double flaws. The flaw geometry was different from that reported in the previous studies. Two flaws with different orientations were made in the PMMA, Diastone, and Hwangdeung granite specimens. The shape of the flaws was similar to the overlapping flaw geometry, and crack coalescence was observed and classified according to the crack coalescence types reported by other researchers. In addition, numerical simulations using PFC^{2D} based on DEM were carried out to model the crack coalescence of the Hwangdeung granite specimens under uniaxial compression.

Only tensile cracks were observed in the PMMA specimens, where coalescence occurred between the adjacent tips when α was smaller than 60° . With increasing α , the coalescence point moved from the upper tip of the inclined flaw to the lower tip of the inclined flaw. Shear cracks and tensile cracks were observed in the Diastone and Hwangdeung granite specimens. The shear cracks were observed after the tensile cracks emerged and caused the specimen failure. A white patch was observed in the Hwangdeung granite specimens, which showed a precedent phenomenon before the crack initiated at that place. However, cracks did not always appear at a place where the white patch emerged. Cracks often appeared without any signs of whitening, even though a white patch propagated from the same tip in a different direction.

The crack initiation and coalescence stresses were analyzed and compared with those of the single flawed specimens of each material. The shielding effect of the horizontal flaw played an important role in the stresses. The crack patterns and stresses reached a critical point when α was approximately 60° , i.e. the inclined flaw was completely under a horizontal flaw. However, further study on the cracking mechanism of the horizontal flaw including the shielding

effect should be carried out for the understanding of the crack initiation and coalescence in the differently oriented flaw geometry. The numerical simulations using PFC^{2D} for Hwangdeung granite were generally in a good agreement with the experimental results (overall cracking behavior).

From the experimental and numerical results, the crack initiation and coalescence in the new flaw geometry were observed and compared with the previously reported results. These results can be used to better understand crack coalescence, which affects the stability of a tunnel, slope and foundation structures that contain cracks or fractures with various orientations and sizes.

Acknowledgement

This work was supported by the National Research Foundation of Korea (NRF) Grant (NRF-F01-2009-000-10100-0).

References

- Bobet, A., 2000. The initiation of secondary cracks in compression. *Engineering Fracture Mechanics* 66, 187–219.
- Bobet, A., Einstein, H.H., 1998a. Fracture coalescence in rock-type materials under uniaxial and biaxial compression. *International Journal of Rock Mechanics and Mining Sciences* 35, 863–888.
- Bobet, A., Einstein, H.H., 1998b. Numerical modeling of fracture coalescence in a model rock material. *International Journal of Fracture* 92, 221–252.
- Bombolakis, E.G., 1968. Photoelastic study of initial stages of brittle fracture in compression. *Tectonophysics* 6, 461–473.
- Cho, N., Martin, C.D., Segol, D.C., 2007. A clumped particle model for rock. *International Journal of Rock Mechanics and Mining Sciences* 44, 997–1010.
- Cundall, P.A., Strack, O.D.L., 1979. A discrete numerical model for granular assemblies. *Geotechnique* 29, 47–65.
- Erdogan, F., Sih, G.C., 1963. On the crack extension path in plates under plane loading and transverse shear. *ASME Journal of Basic Engineering* 85, 519–527.
- Hoek, E., Bieniawski, Z.T., 1965. Brittle fracture propagation in rock under compression. *International Journal of Fracture* 1, 137–155.
- Hussain, M.A., Pu, E.L., Underwood, J.H., 1974. Strain energy release rate for a crack under combined mode I and mode II. In: *Fracture Analysis*. ASTM STP 560. American Society for Testing and Materials, pp. 2–28.
- Ingraffea, A.R., Heuze, F.E., 1980. Finite element models for rock fracture mechanics. *International Journal of Numerical and Analytical Methods in Geomechanics* 4, 25–43.
- Itasca, C.G., 2002. *Users' Manual for Particle Flow Code in 2 Dimensions (PFC2D)*, Version 3.1, Minneapolis Minnesota.
- Jiefan, H., Ganglin, C., Yonghong, Z., Ren, W., 1990. An experimental study of the strain field development prior to failure of a marble plate under compression. *Tectonophysics* 175, 184–269.
- Jong, Y.H., Lee, C.I., 2006. Suggested method for determining a complete set of micro-parameters quantitatively in PFC2D. Tunnel and underground space. *Journal of Korean Society for Rock Mechanics* 16, 334–346 (in Korean).
- Kranz, R.L., 1979. Crack-crack and crack-pore interactions in stressed granite. *International Journal of Rock Mechanics and Mining Sciences and Geomechanics Abstracts* 16, 37–47.
- Lajtai, E.Z., Carter, B.J., Duncan, E.J.S., 1994. En echelon crack-arrays in Postash salt rock. *Rock Mechanics and Rock Engineering* 27, 89–111.
- Lajtai, E.Z., 1971. A theoretical and experimental evaluation of the Griffith theory of brittle fracture. *Tectonophysics* 11, 129–156.

- Lajtai, E.Z., 1974. Brittle fractures in compression. *International Journal of Fracture* 10, 525–536.
- Li, Y.P., Chen, L.Z., Wang, Y.H., 2005. Experimental research on pre-cracked marble under compression. *International Journal of Solids and Structures* 42, 2505–2516.
- Mandal, N., 1995. Mode of development of sigmoidal en echelon fractures. *Journal of Earth Systems Science* 104, 454–464.
- Miller, J.T., Einstein, H.H., 2008. Crack coalescence tests on granite. In: *Proceedings of 42nd US Rock Mechanics Symposium, ARMA 08–162*, San Francisco.
- Mughieda, O., Alzo'ubi, A.K., 2004. Fracture mechanisms of offset rock joints – a laboratory investigation. *Geotechnical and Geological Engineering* 22, 545–562.
- Park, N.S., 2001. Crack Propagation and Coalescence in Rock Under Uniaxial Compression. Master's Thesis, Seoul National University.
- Potyondy, D.O., Cundall, P.A., 2004. A bonded-particle model for rock. *International Journal of Rock Mechanics and Mining Sciences* 41, 1329–1364.
- Reyes, O., Einstein, H.H., 1991. Failure mechanisms of fractured rock – A fracture coalescence model. In: *Proceedings of 7th Congress of the ISRM, Aachen, Germany*, pp. 333–340.
- Roering, C., 1968. The geometrical significance of natural en-echelon crack-arrays. *Tectonophysics* 5, 107–123.
- Sagong, M., Bobet, A., 2002. Coalescence of multiple flaws in a rock-model material in uniaxial compression. *International Journal of Rock Mechanics and Mining Sciences* 39, 229–241.
- Shen, B., 1995. The mechanism of fracture coalescence in compression-experimental study and numerical simulation. *Engineering Fracture Mechanics* 51, 73–85.
- Shen, B., Stephansson, O., 1994. Modification of the G-criterion for crack propagation subjected to compression. *Engineering Fracture Mechanics* 47, 177–189.
- Sih, G.C., 1974. Strain-energy-density factor applied to mixed mode crack problems. *International Journal of Fracture* 10, 305–321.
- Tang, C.A., Kou, S.Q., 1998. Crack propagation and coalescence in brittle materials under compression. *Engineering Fracture Mechanics* 61, 311–324.
- Tang, C.A., Lin, P., Wong, R.H.C., Chau, K.T., 2001. Analysis of crack coalescence in rock-like materials containing three flaws – Part II: Numerical approach. *International Journal of Rock Mechanics and Mining Sciences* 38, 925–939.
- Vallejo, L.E., 1987. The influence of fissures in a stiff clay subjected to direct shear. *Geotechnique* 37, 69–82.
- Vallejo, L.E., 1988. The brittle and ductile behavior of clay samples containing a crack under mixed mode loading. *Theoretical and Applied Fracture Mechanics* 10, 73–78.
- Vásárhelyi, B., Bobet, A., 2000. Modeling of crack initiation, propagation and coalescence in uniaxial compression. *Rock Mechanics and Rock Engineering* 33, 119–139.
- Vesga, L.F., Vallejo, L.E., Lobo-Guerrero, S., 2008. DEM analysis of the crack propagation in brittle clays under uniaxial compression tests. *International Journal for Numerical and Analytical Methods in Geomechanics* 32, 1405–1415.
- Wang, R., Zhao, Y., Chen, Y., Yan, H., Yin, Y.Q., Yao, C.Y., Zhang, H., 1987. Experimental and finite simulation of X-shear fractures from a crack in marble. *Tectonophysics* 144, 141–150.
- Wong, R.H.C., Chau, K.T., 1998. Crack coalescence in a rock-like material containing two cracks. *International Journal of Rock Mechanics and Mining Sciences* 35, 147–164.
- Wong, L.N.Y., Einstein, H.H., 2008a. Crack coalescence in molded gypsum and Carrara marble: Part 1. Macroscopic observations and interpretation. *Rock Mechanics and Rock Engineering* 42, 475–511.
- Wong, L.N.Y., Einstein, H.H., 2008b. Crack coalescence in molded gypsum and Carrara marble: Part 2. Microscopic observations and interpretation. *Rock Mechanics and Rock Engineering* 42, 513–545.
- Wong, L.N.Y., Einstein, H.H., 2009. Systematic evaluation of cracking behavior in specimens containing single flaws under uniaxial compression. *International Journal of Rock Mechanics and Mining Sciences* 46, 239–249.
- Wong, R.H.C., Chau, K.T., Tang, C.A., Lin, P., 2001. Analysis of crack coalescence in rock-like materials containing three flaws – Part I: Experimental approach. *International Journal of Rock Mechanics and Mining Sciences* 38, 909–924.
- Wong, R.H.C., Guo, Y.S.H., Liu, L.Q., Liu, P.X., Ma, S.P., 2008. Nucleation and growth of anti-wing crack from tips of strike-slip flaw. In: *Proceedings of 42nd US Rock Mechanics Symposium, ARMA 08–23*, San Francisco.
- Yoon, J., 2007. Application of experimental design and optimization to PFC model calibration in uniaxial compression simulation. *International Journal of Rock Mechanics and Mining Sciences* 44, 871–889.



Heekwang Lee is currently a Ph.D. student in the School of Civil, Urban and Geosystem Engineering at Seoul National University, Seoul, Korea. He received his Bachelor's and Master's degree in the School of Civil, Urban and Geosystem Engineering, Seoul National University in 2001 and 2003, respectively. His research interests are rock mechanics, blasting, and numerical simulations, etc.



Seokwon Jeon is currently an Associate Professor in the Department of Energy Systems Engineering at Seoul National University, Seoul, Korea. He is also Director of Research Institute of Energy Resources Engineering. He received his Bachelor's and Master's degree in the Department of Mineral and Petroleum Engineering, Seoul National University in 1987 and 1989, respectively. In 1996, he received his Ph.D. degree in the Department of Mining and Geological Engineering, the University of Arizona. He joined Seoul National University as a faculty member in 1997. His research interests are experimental rock mechanics, rock

dynamics, blasting, etc.